Eidgenössische Technische Hochschule Zürich
Swiss Federal Institute of Technology Zurich

Master Thesis

Commissioning and Charge Readout Calibration of a 5 Ton Dual Phase Liquid Argon TPC

by

Caspar Schlösser

April, 2017

Supervisor: Prof. Dr. André Rubbia

Department of Physics, ETH Zurich

Contents

List of Figures

List of Tables

Abstract

Dual phase time projection chambers with amplification of ionization electrons provide a novel technique for measuring and analyzing rare events with excellent spatial resolution and great calorimetric properties. This thesis describes the commissioning of the WA105 $3 \times 1 \times 1$ m^3 dual phase liquid argon detector, built to demonstrate the performance of this kind of detector on large scales in order to determine the viability of giant dual phase time projection chambers in long baseline neutrino oscillation experiments. The properties of the insulation and the main tank vessel are described and analyzed, such as the pressure, temperature and argon purity requirements during operation in order to guarantee stable conditions and good event tracking. As signals are induced due to electrons from ionizing radiation, crosstalk is caused by capacitive couplings between strips of the charge readout plane and in the electronics of the data acquisition. These induced signals are studied and compared to capacitance and pulsing measurements on one anode module and an equivalent circuit model is introduced to quantitatively describe this crosstalk.

Acknowledgements

First and foremost I would like to express my sincere gratitude to my advisor, Prof. Dr. André Rubbia for the opportunity to work in his group on this stimulating project. I would like to thank Dr. Sebastien Murphy for his guidance and effort to further my understanding of experimental physics and his support during my time at CERN. I am also very grateful to Dr. Laura Molina Bueno, Cosimo Cantini, Dr. François Duval, Yann-Axel Franck Rigaut and Dr. Christian Regenfus with whom I had very stimulating discussions. Their experience provided me with valuable insights and helped me advance in my methodology and approach to experiments. Of great help have been Christoph Alt, Shuoxing Wu, Dr. Animesh Chatterjee and Thierry Viant and I would like to thank them for their valuable insights. Rita Vonesch was of great help in the administrative formalities during my arrival in Geneva. Working with Pin-Jung Chiu and Kevin Fusshoeller has been a great pleasure and I am thankful for their contributions and our successful collaboration.

Abbreviations used

CERN: European Organization for Nuclear Research
TPC: time projection chamber
LAr: liquid argon
CRP: charge readout plane
VUV: vacuum ultraviolet (wavelength between 10-200 nm)
PMT: photomultiplier tube
LEM: large electron multiplier
PCB: printed circuit board
SNR: signal-to-noise ratio
RMS: root mean squared
ENC: equivalent noise charge
MIP: minimum ionizing particle
FFT: fast Fourier transform
LBNO: long baseline neutrino oscillation
LSC: Laboratorio Suberráneo de Canfranc
SGFT: signal feedthrough
IS: insulation space
SCFT: slow control feedthrough
ADC: analog-to-digital converter

Chapter 1

Introduction

The $3 \times 1 \times 1$ m^3 dual phase liquid argon time projection chamber is the largest ever built detector of its kind, providing electron multiplication, with a total liquid argon mass of 24 tons and a charge readout plane of 3×1 m^2. I was involved in the commissioning of the detector, located in building 182 in the CERN west area. During this time, I investigated the quality of the passive insulation and determined the heat input during the first cool down as well as the expected one during operation. As air gaps were found in the insulation, the cool down could not be completed up to the required 87 K of liquid argon temperature and the insulation needed to be fixed. I also worked on ensuring that all closed volumes that are in contact with the cold membrane vessel, such as the cryostat's passive insulation and the signal feedthrough chimneys, are properly purged with nitrogen to avoid the risk of having oxygen liquefy. The methods used revealed what steps need to be taken to scale up to larger dual phase time projection chambers in the future. To achieve good results (long drift lengths and stable gains), the impurities in the liquid argon need to be kept to a minimum and the pressure needs to be kept extremely stable. The achievement of both these requirements is described in detail.

The signal-to-noise ratio for a minimum ionizing particle was found to be 130 with an expected root mean squared value of the noise of 1500 electrons and assuming a gain of 20, which is the previously achieved constant gain. Impurity levels of 0.2, 3.5 and 25 ppm were achieved after purging the detector in open and closed loop for oxygen, nitrogen and moisture respectively.

This detector serves as a prototype to determine if larger TPCs are feasible for future neutrino, dark matter and proton decay experiments. Problems observed and lessons learned for the upcoming $6 \times 6 \times 6$ m^3 detector are reported and given in the conclusion.

The last chapter before the conclusion of my thesis focuses on the level of noise achieved during noise measurements performed before the cool down. A low pass filter, using the Fourier transform of the signals, was also explored to improve the signal quality and achieve a better signal-to-noise ratio. Its effect on signal waveforms was also studied. In addition, the Fourier transformed signals provide a means to identify frequencies induced by noise and can thus provide information on the source of the noise. Additionally, pulsing measurements were also performed on the anode in the detector using a pulse with a known amount of charge to study its response and determine the amount of crosstalk induced on other strips of the anode. The induced crosstalk was studied in detail and in order to gain a better understanding of it, capacitance measurements were performed on a single anode module. These were used to build an equivalent circuit model of one strip of the anode with a capacitive coupling to another strip and to the rest of the detector which was compared to pulsing measurements on the anode module, where a single strip was pulsed and the response of other strips was measured. The results found give an explanation for the induced crosstalk, seen during the pulsing measurements of the anode.

Chapter 2

Dual phase time projection chambers for rare event detection

In this chapter, the general principle of time projection chambers (TPCs) is introduced and described. Then the properties of liquid argon (LAr) are described as well as why it is a good choice for TPCs. Then the single and dual phase TPCs are introduced and compared to each other, followed by a list of detectors employing this principle and the challenges that arise in building larger detectors.

2.1 Principle of time projection chambers

The TPC is a type of particle detector, which was invented in 1974 by David Nygren [1]. It consists of an active volume, filled with an ionizable medium, with a uniform electric field applied throughout it. As an ionizing particle passes through the detector, it deposits its energy in the active volume by creating electron-ion pairs. Subsequently, the electrons drift along the electric field lines towards the anode of the detector, the positively charged ions drift in the opposite direction towards the cathode. The electrons are collected on a segmented anode and produce current pulses proportional to the charge collected and thus to the energy loss of the ionizing particle. The position of pulsed anode strips gives the x and y coordinates of the event track, projected onto the charge readout plane (CRP). These 2D coordinates as well as the arrival times of the electrons are used to reconstruct the 3D event track, as the drift velocity along the z axis remains constant within the medium, due to the uniform electric field. The local dE/dx information is obtained from the deposited charge and thus provides a means for particle identification.

2.2 Liquid argon as active medium

In 1977 Carlo Rubbia proposed the idea of using liquid argon as the active medium in TPCs [2]. The advantages of LAr include its high density of $\rho_{LAr} = 1.4$ g/cm^3, thus providing superior calorimetric properties, its high electron mobility and low diffusion along the drift path, leaving the electron distribution relatively unaltered, as described below. Relevant intrinsic LAr properties are summarized in Table 2.1. Argon is chemically inactive and can be rather

Property	**Value**	**Unit**
atomic number	18	
standard atomic weight	39.948	g/mol
boiling point at 1 atm	87.303	K
liquid density at boiling point	1.369	g/cm^3
latent heat of vaporisation	161.14	kJ/kg
ionisation energy W [3]	$23.6^{+0.5}_{-0.5}$	eV
electron drift velocity at 500 V/cm (1 kV/cm)[4]	1.648 (2.261)	mm/μs
ion drift velocity ($\mathcal{E}_{\text{drift}} < 1$ kV/cm) [5]	8	mm/s
average energy loss for a MIP	2.1	MeV/cm
radiation length	19.55	g/cm^2
nuclear interaction length	119.7	g/cm^2
Molière radius	12.62	g/cm^2
scintillation wavelength (dominant component)	128	nm
attenuation after 1 m (6 m) drift ($\mathcal{E}_{\text{drift}} < 1$ kV/cm, 100 ppt oxygen equivalent impurities)	13.7 (58.7)	%

Table 2.1: Physical, chemical and thermodynamical properties of argon.

easily purified to a level of $\mathcal{O}(10$ ppt). It is abundant in the atmosphere, making up about 1 %, thus providing a relatively cheap alternative to other ionization media as it can be easily obtained as a byproduct of the air liquefaction process.

The VUV scintillation light of LAr, due to excitations and subsequent de-excitations of argon atoms, can be exploited and used as a high efficiency trigger in order to obtain the absolute time of an event. LAr has excellent scintillation properties with about 40000 photons/MeV of energy deposited in a drift field of 0.5 kV/cm [6]. The scintillation light has a peak wavelength of 128 nm, which LAr is transparent to. However, conventional glass or crystal photomultiplier tube (PMT) windows are not transparent to the scintillation light, thus windows from other materials such as MgF_2 or wavelength shifters have to be employed in order to increase the wavelength of the photons.

Long drift paths are possible in LAr TPCs, as the electron diffusion in both the longitudinal and transversal directions is only of the order of a few millimeters for drifts of several meters [4], if a sufficiently high purity is achieved. As the electrons drift towards the anode, they may be captured by electronegative molecules, such as O_2, H_2O and N_2, dissolved in the liquid argon. After capturing the electrons, these molecules become negatively charged ions that drift to the anode at a drift speed three orders of magnitude lower than the drift speed of free electrons. This leads to a reduction of the measured signal as the captured electrons do not contribute, leading to impurity dependent attenuation over long distances. With $n_e(t)$ and n_i giving the number of surviving electrons and the impurity concentrations for various contaminants respectively, the dynamical behavior of free electrons is given by:

$$\frac{dn_e}{dt} = -\sum_i k_i \cdot n_i \cdot n_e \tag{2.1}$$

where k_i are the respective attachment coefficients, proportional to the attachment cross section. Thus, the amount of surviving electrons after drift time t is given by:

$$n_e(t) = n_{e0} e^{-t/\tau} \tag{2.2}$$

where n_{e0} is the initial number of electrons and $\tau = 1/\sum_i k_i n_i$ is defined as the electron lifetime. An estimation of τ is usually given using the oxygen equivalent impurity concentration [7]:

$$\tau[\mu s] \approx \frac{300}{[O_2][ppb]} \tag{2.3}$$

Thus, for an oxygen equivalent impurity concentration of 100 ppt, the electron lifetime is 3 ms. This time corresponds to a drift length of 5 m with a drift field of 0.5 kV/cm.

Thus LAr TPCs offer a dense, sensitive and uniform active volume and have the capabilities of reproducing 3D event tracks with millimetric granularity for drifts of several meters, as the initial charge distribution remains relatively constant, both in shape and quantity for sufficiently high purities. Particle identification is obtained from the local dE/dx information, with the LAr TPC providing a homogeneous full sampling calorimeter with excellent energy resolution over a wide range of energies. These features make it an ideal candidate for future giant detectors for neutrino experiments, dark matter searches and proton decay studies which require good background discrimination, achieved through the excellent imaging capabilities.

2.3 The liquid argon time projection chamber

LAr TPCs consist of an active volume filled with liquid argon, with a uniform electric field applied through the LAr bulk, with field strengths of 0.5-1.0 kV/cm. The field is required to drift the ionization electrons, created by ionizing particles passing through the active volume, towards the anode at a speed of 1.6 mm/μs for a drift field of 0.5 kV/cm. By measuring the scintillation light produced by the ionizing particle using PMTs located inside the detector, the absolute time of the event can be obtained with an accuracy of a few nanoseconds. LAr TPCs can be classified into two different categories: single phase and dual phase TPCs, described below.

2.3.1 Single phase LAr TPCs

For single phase TPCs such as the ICARUS T600 detector [16], the drift electrons are read out on multiple planes with sets of parallel wires, located at one end of the detector within the liquid. These sets are called views, and provide the projection of the x and y coordinates onto the CRP. The different planes are composed of sets of parallel wires, having an appropriate voltage bias, such that the electrons induce a bipolar signal on the first planes, called induction views, in non-destructive ways and are collected on the last plane, the collection view, producing a unipolar signal. The drift time in the liquid is proportional to the z coordinate of the event, with the z axis being parallel to the drift field. The signals of the PMTs provide an additional datum, the reference time for each event, which is used as a high efficiency trigger. Thus, the three dimensional tracks can be reconstructed with a uniform spatial resolution of about 1 mm^3 in the case of the ICARUS T600 detector over an active volume of 170 m^3 [8].

2.3.2 Dual phase LAr TPCs

Just like the single phase TPC, described in 2.3.1, the dual phase LAr TPC consists of a LAr active volume with a drift field of about 0.5-1-0 kV/cm orientated from top to bottom and PMTs, located inside the detector, providing a trigger datum for each event. First proposed in 2004 [9], the LAr dual phase TPC, in contast to the single phase TPC, employs a gas layer of argon, located above the active volume, consisting of LAr. Once the electrons reach the top of the liquid, they are extracted into the vapor phase suing an appropriately high electric field of about 2 kV/cm, created by an extraction grid, located a few millimeters below the LAr surface. Once extracted into the gas phase, the electrons can be multiplied using so-called large electron multipliers (LEMs), 1 mm thin printed circuit board (PCB) structures with macroscopic holes of diameter of about 0.5 mm, with a very high electric field established within the holes of about 30 kV/cm. As the electrons pass through the holes, they are accelerated and ionize further argon atoms, leading to a cascade known as a Townsend avalanche, described below. A schematic overview of the operation principle of dual phase TPCs is given in Figure 2.1. As the ionization charges produced in rare events such as neutrino interactions can be very

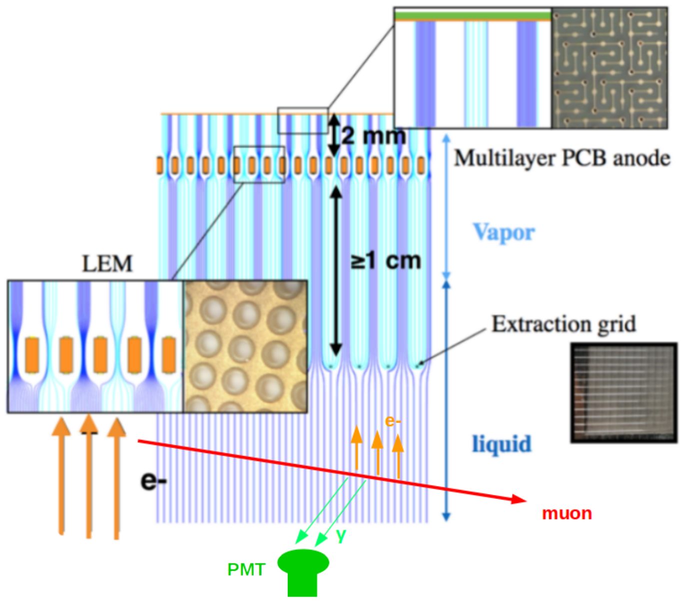

Figure 2.1: Schematic of the operation principle of dual phase LEM-TPCs. As ionizing particles traverse the active volume (liquid), electrons are released, drifting along the field lines to the top of the detector where they are extracted into the vapor phase, multiplied in the LEMs and collected on the anode. In addition, the produced scintillation light can be used as a trigger, using PMTs inside the detector.

small, the amplification achieved through the electron multiplication in the LEMs provides a means for obtaining a better signal-to-noise ratio (SNR). Thus particles at lower energy thresholds can be tracked more efficiently.

Extraction into the vapor phase

The electrons produced by the ionizing event drift along the field lines to the top of the liquid, where they are extracted into the vapor phase using a relatively high electric field of ≥ 2.0 kV/cm (compared to the 0.5-1.0 kV/cm drift field) with a close to 100 % efficiency. This electric field is provided by an extraction grid, positioned a few millimeters below the LAr surface. This design allows to establish the required extraction field independently of the drift field. When extracting the electrons from the liquid, the following conditions must be met: the electrons must not be collected on the grid, to eliminate any further attenuation of the signal, and the spatial distribution of the charges must remain the same before and after the grid, to avoid image distortions in the 3D track reconstruction. These conditions can be met using a grid consisting of sets of thin parallel conducting wires with fixed pitch of a few millimeters, with the sets being perpendicular to each other and in the horizontal plane. The two sets must be parallel to the surface of the liquid to establish a uniform field on it, with wires in each set being well aligned and both sets exactly one on top of the other. Once extracted, the electrons drift towards the LEMs, located in the vapor phase where they are multiplied due to the very high electric field within the LEM holes, as described below.

LEM gain and Townsend avalanche

The LEM, located in the gas phase below the anode, provides the means for multiplying the extracted electrons in the argon gas phase and thus obtaining a larger charge from the ionizing event, enabling higher detector sensitivities and better 3D reconstruction. It constitutes a macroscopic sturdy structure, can be manufactured using standard PCB techniques and consists of a 1 mm thick glass epoxy plate, coated with copper on both sides. Macroscopic holes of diameter 0.5 mm are drilled into the plate, with a pitch of 0.8 mm. A schematic of the LEM and the electric field lines passing through it and a picture of the top are shown in Figure 2.2. An very high electric field of 30 kV/cm is applied across the holes of the LEM

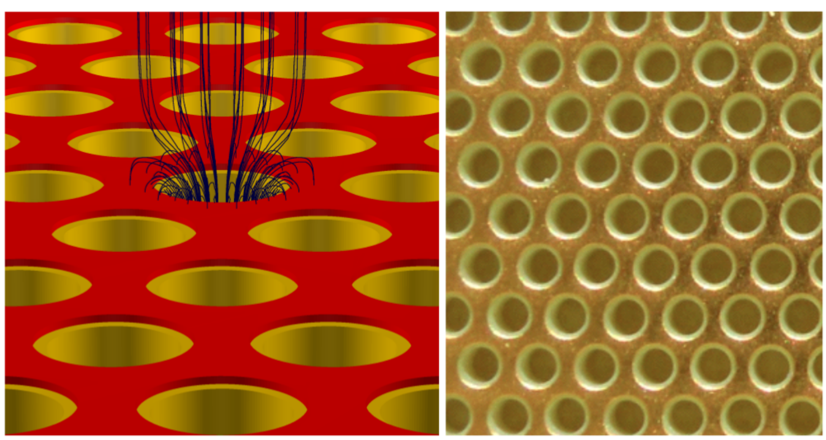

Figure 2.2: Left: schematic drawing of the LEM, consisting of the copper electrodes (red) and the insulating material FR4 (yellow). The field lines passing through the central hole are drawn in blue. Right: closeup picture of a manufactured LEM. As in the schematic drawing on the left, the dielectric rim is clearly visible.

(compared to the drift field of 0.5-1.0 kV/cm). Within the LEM holes, the drift electrons are accelerated due to the increasing electric field, and can thus ionize further neutral atoms within the argon gas if their kinetic energy exceeds the respective ionization energy. As these liberated secondary electrons can induce further ionization, a cascading effect occurs, known as a Townsend avalanche. The first Townsend ionization coefficient α gives the number of electron-ion pairs n generated per unit length by a drift electron. Thus the dynamical behavior of the number of electrons is given by:

$$\frac{dn}{dx} = \alpha n \tag{2.4}$$

For a constant uniform amplification field and thus $\alpha = const$, the obtained solution is:

$$n = n_0 e^{\alpha x} \tag{2.5}$$

where n_0 is the number of electrons extracted from the liquid before the multiplication in the LEMs. A very useful empirical parametrization of the first Townsend ionization coefficient is given by:

$$\alpha = A \cdot \rho \cdot \exp\left[-\frac{B\rho}{\mathcal{E}}\right] \tag{2.6}$$

which depends on the electric field $\mathcal{E}$, the gas density ρ and the two gas specific constants A and B. The effective gain G_{eff} of the detector is defined as:

$$G_{eff} = \frac{n}{n_0} \tag{2.7}$$

In a previous small scale 3 liter LAr dual phase TPC, a stable effective gain of $G_{eff} = 20$ was obtained [10].

As the Townsend coefficient strongly depends on the gas density ρ, it is imperative to be able to keep the pressure inside the cryostat constant in order to achieve a stable gain. One of the objectives of this thesis is to investigate the behavior of the pressure in the cryostat with changing atmospheric pressure and determine whether a constant tank pressure can be retained in the operational mode of the detector, see Section 4.1 for more details.

Charge collection and readout

After the electrons have been extracted from the liquid phase and multiplied in the LEMs, they are finally collected on a segmented anode, a standard PCB, composed of at least two sets of readout strips, called views. For the case of having two views, the two sets of strips are perpendicular to each other. The strips have a pitch of a few millimeters to allow for precise reconstruction of the event coordinates, and are separated from each other by a thin insulating layer. A picture of the anode employed in the $3 \times 1 \times 1$ m^3 dual phase detector as well as its schematic and interconnections are given in Figure 2.3 and a detailed description

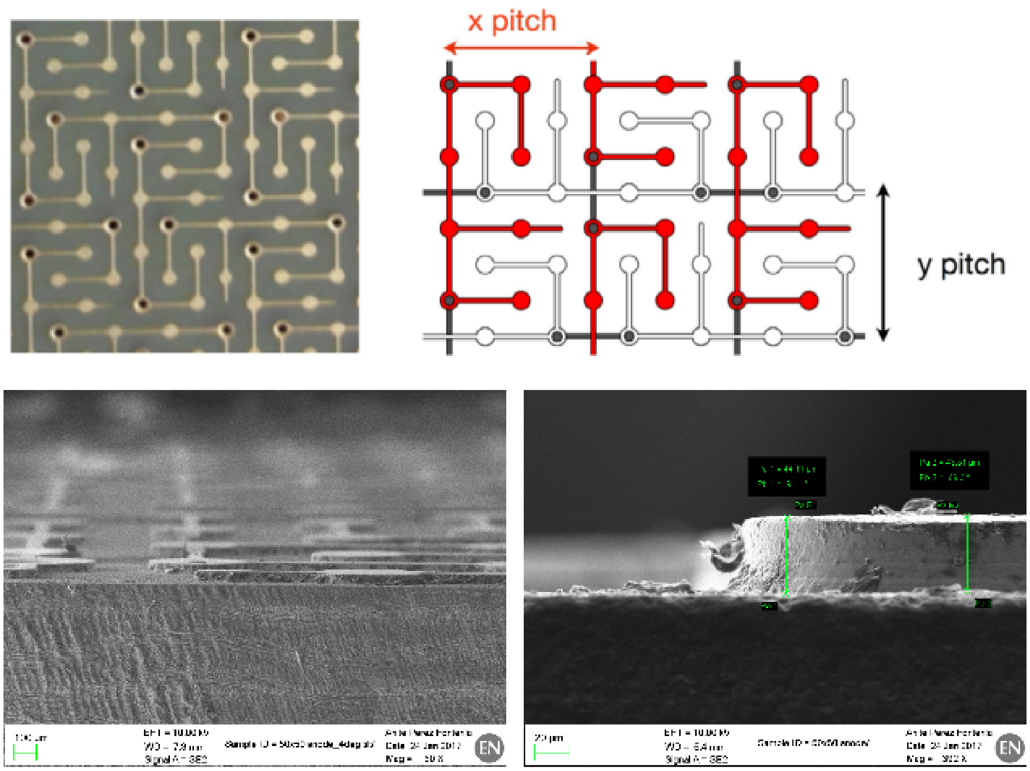

Figure 2.3: Top Left: Close-up picture of the anode employed in the $3 \times 1 \times 1$ m^3 detector, showing the track pattern of the copper strips that allows a two view readout on the same circuit board with equal charge sharing between the views. Top Right: Schematic explaining the interconnections between both views (filled in red and white). The 3.125 mm readout pitches are indicated by arrows. Bottom: Images from a scanning electron microscope of the strip layout on the anode.

is provided in Section 3.2. A symmetric design of the anode with respect to the two views ensures equal charge splitting of the arriving electrons, which are collected in both views. This collected charge on the anode strips can be measured using charge sensitive preamplifiers and is proportional to the deposited energy of the particle. Thus the local energy loss rate dE/dx can be obtained, providing the information necessary for identification of the particles. By segmenting the anode into separate sets of electrode strips, the 2D coordinates of the projection of the particle track onto the CRP can be obtained. These x and y coordinates as well as the arrival times of the electrons make 3D track reconstruction possible, as the drift velocity along the z axis remains constant within the LAr up to the extraction grid, due to the uniform electric field. Thus the z coordinate of the event is proportional to the drift time. An additional datum, the absolute time of the event, can be obtained from the scintillation light produced by the ionizing particles, detected in the PMTs as described above. Therefore, TPCs can be used to reconstruct the three-dimensional particle tracks with high spatial resolution of a few millimeters, an intrinsically high time resolution and high multitrack efficiency as well as measurement of the local dE/dx information to allow for particle identification.

Having a symmetric split between both views of the anode simplifies the extraction of the signal waveforms as well as the event reconstruction process. In previous designs for a 3 liter dual phase LAr LEM TPC prototype [11], charge sharing was achieved by employing an anode consisting of two orthogonal sets of copper strips interleaved with a 50 μm thick Kapton insulator. The measured capacitances per unit length were as high as 600 pF/m for this type of anode, due to the proximity of the copper strips [12]. As reported in [13], the measured root mean squared (RMS) value of the equivalent noise charge (ENC) for a total capacity of 480 pF at the input of the preamplifiers is 1420 $\pm$ 30 e^-. In order to ensure a SNR of at least 10 for minimum ionizing particle (MIP) tracks, the capacitances of strips on the anode should not exceed values of about 500 pF. This thesis offers an analysis of the capacitive couplings between the strips on the currently employed anode in the $3 \times 1 \times 1$ m^3 detector, designed to have a capacitance per unit length of 150 pF/m. A detailed description and analysis of the observed noise levels and signals induced through cross capacitances between the strips can be found in Chapter 5.

2.3.3 Advantages of dual phase over single phase

The advantages of dual phase argon LEM TPCs over single phase ones include the greater number of electrons reaching the anode due to the multiplication in the LEM thus leading to a much improved SNR. In addition the calorimetric properties of the detector are superior, due to the high density of the LAr (1400 kg/m^3). The absolute time of each event can be obtained from the scintillation light, which combined with the induced signals on the segmented anode, gives excellent 3D reconstruction with millimetric granularity, as the strip pitch is only a few millimeters. As the anode is located in the gas phase and can be designed with symmetric views, the signals induced in each view are equivalent. Thus, no complicated deconvolution of induction and collection wire signals is needed, as in the case of single phase TPCs. Additionally, the signal degradation is small over drift lengths of several meters, provided a sufficiently high purity of the liquid has been achieved as described in Section 2.2.

2.4 Signals and recorded events from previous TPC detectors

An ionizing event in a LAr TPC is generally represented as the one shown in Figure 2.4. The

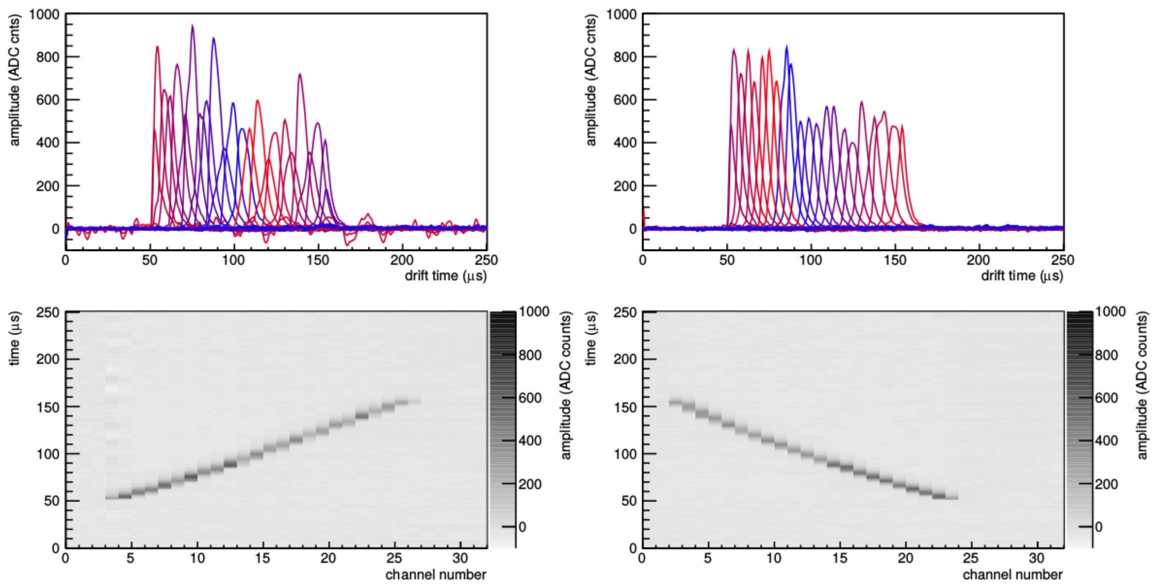

Figure 2.4: Top: Waveforms recorded on different strips from the ionizing event for the two views. Bottom: Charge recorded on the anode strips as a function of the drift time, with the gray scale corresponding the intensity. Shown are the signals for the two views. [14].

event shown corresponds the signals obtained from a cosmic muon traversing a 3 liter dual phase LAr TPC with a gain of 20 [14], with the charge recorded on each strip being plotted in gray scale according to the signal amplitude, against time and channel number. The reconstruction of the 3D particle track is done using the specially designed Qscan software, able to subtract coherent noise and implement noise filters using fast Fourier transform (FFT) algorithms. Combining the signals from both views enables the reconstruction of the 3D track. Physical hits are discriminated from the ambient noise using peak finding algorithms. The waveform integral is proportional to the charge deposited on one anode strip and thus gives a measure of the local dE/dx information, needed for identification of particles with straight tracks such as muons. Other particles producing electromagnetic (e^-, γ) or hadronic ($\pi^\pm, K^\pm$) showers are identified through their characteristic event topologies. Figure 2.5 shows one such event in the case of a nuclear break up, taken from the same 3 liter TPC, described above [14].

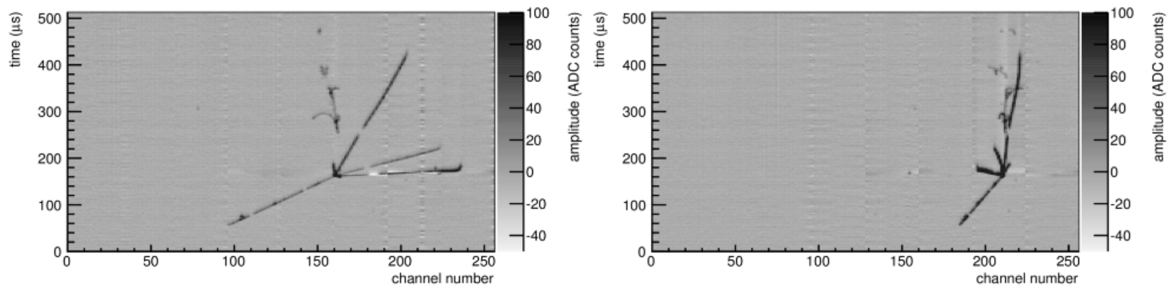

Figure 2.5: The two views of a nuclear breakup, recorded in a 3 liter LAr dual phase TPC [14].

Detector	**Type**	**Mass**	**Physics**
50 L [15]	single phase	65 kg	neutrino cross section, quasielastic interaction
ICARUS T600 [16]	single phase	760 ton	neutrino cross section, neutrino oscillation, astrophysical neutrinos
ArDM [17]	dual phase	850 kg	Dark Matter
MicroBooNE [18]	single phase	80 ton	neutrino cross sections, neutrino oscillation
GLACIER [19] (proposed)	dual phase	100 kton	neutrino oscillations, CP-violation, proton decay

Table 2.2: Summary of experiments employing the LAr TPC technology.

2.5 Present and future LAr TPCs

Following the idea of Carlo Rubbia in 1977 [2] of using LAr as the active volume in conventional single phase TPCs, and thus enabling it to act as a sampling calorimeter with excellent energy resolution, various single phase LAr TPCs have been constructed and successfully operated. The ICARUS collaboration for instance has successfully operated the T600 detector [16], filled with 760 tons of ultra-pure LAr (impurities below 100 ppt) and capable of achieving a SNR of 10 for MIPs [8]. It constitutes the largest LAr TPC ever built thus far. Hence, the single phase LAr TPC is considered a mature technology, with multi-kiloton detectors having been successfully employed in neutrino and astroparticle physics experiments.

The usage of dual phase TPCs allows for amplification of the electrons in the LEMs with stable gains of 20 reported [10] and thus the capabilities of achieving a higher SNR. Over the past years, dual phase TPCs at the scale of multiple liters have been constructed and successfully operated [20]. The main objectives of these prototypes has been the optimization of the readout electronics, to study the gains that can be achieved with stable conditions and to investigate the feasibility of larger dual phase TPCs at the multi-ton and multi-kiloton level. Employing the LAr dual phase LEM TPC design has been proposed for future giant detectors employed as the far detector in long baseline neutrino oscillation (LBNO) experiments, such as DUNE [21], a proposed 40 kton underground detector. The $3 \times 1 \times 1$ m^3 detector, whose commissioning is described in this thesis, and a much larger $6 \times 6 \times 6$ m^3 dual phase LEM TPC, with an active mass of 300 tons, currently being constructed at CERN and aiming to take data in 2018, serve as prototypes to investigate the performance at these scales and scalability of the dual phase technology. While the $3 \times 1 \times 1$ m^3 detector will be solely exposed to cosmic rays, the $6 \times 6 \times 6$ m^3 will be exposed to charged particles from a beam with adjustable particle types and energies.

Of great interest is the performance of the anodes employed in terms of minimizing noise and studying the crosstalk between channels, the ability to achieve a stable gain and the realization of $< \mathcal{O}(100ppt)$ impurity levels for tank vessels of this size. This thesis covers the evolution of impurities during the commissioning currently taking place, the thermodynamic behavior of the tank and a quantitative analysis of the noise and crosstalk due to capacitive couplings between strips on the anode of the $3 \times 1 \times 1$ m^3 detector, see Sections 4.3, 4.4 and 5.3 respectively.

The dual phase TPC principle is also suited for studying Dark Matter weak interactions and potential proton decays. ArDM [17], a direct Dark Matter search experiment employing cryostat with a LAr mass of 1 ton, located 850 m underground in the Laboratorio Suberráneo de Canfranc (LSC), is pioneering the dual phase LAr LEM TPC technology, with maximum drift lengths of 1.1 m. This technology also extends to future experiments with active volumes of multiple kilotons, such as the proposed GLACIER detector [19], expected to study proton decays and act as the far detector in LBNO experiments with an proposed active volume of 100 kton. The DUNE far detector will be used in a LBNO experiment, and study the appearance/disappearance of different neutrino types, produced at Fermilab after their propagation of 1300 km. It is expected to be segmented into four detectors, each with a mass around 10 kilotons. A list of some LAr TPCs can be found in Table 2.2.

2.6 Challenges in scaling up to larger TPCs

One of the conclusions drawn from the research and development into the proposed multi-kiloton dual phase TPCs concerns the performance of the charge readout modules on the scale of multiple square meters. Each module consists of the extraction grid, guaranteeing the efficient extraction of electrons from the liquid into the gas, the LEM, used to multiply the electrons in Townsend avalanches due to a high electric field, and the anode, consisting of two sets of parallel strips (or views), which are perpendicular to each other to allow for event reconstruction. As the strips in each view have a pitch of a few millimeters between each other, cross capacitances between the strips are of great concern, when operating at charge levels of only a few fC. One of the objectives of this thesis is to investigate the induced signals on neighboring strips resulting from the capacitive couplings, described in detail in Section 5.3. In order to guarantee a SNR of at least 10, which is the required minimum for good 3D reconstruction of event tracks, the ENC introduced from capacitive couplings should be of order 1500 electrons.
This places a limit on the maximum capacitance of one each strip to all other components of the detector of about 500 pF, as described in Section 2.3.2. The anodes employed in the $3 \times 1 \times 1$ m^3 detector were primarily designed with the objectives of ensuring equal charge sharing between the two views and a low capacitance between each strip and the detector. Having measured this capacitance per unit length to be 156 pF/m, as described in Section 5.4, this means that the maximum length of strips should not exceed 3 m to guarantee the required SNR. Thus the maximum size of the employed CRPs in future LAr dual phase TPCs is of the order 3×3 m^2. It is attractive to have long strips, as opposed to multiple shorter ones, as it requires less readout electronics and reduces the number of signal feedthrough (SGFT) chimneys, which are specially designed chimneys on top of the CRP, providing a housing for the preamps and readout electronics. The great advantage of having the preamps in the SGFT chimneys is the easy accessibility from outside the detector, as the chimneys themselves constitute a separate volume from the active volume in the detector. A more inclusive description of the chimneys is given in Section 3.3. As each chimney can only house readout modules for a few hundred strips, it is attractive to minimize the number of strips and and thus chimneys to keep the costs down and increase usable space.

Another challenge resulting from scaling up to bigger LAr TPC cryostats arises from the requirement of achieving and maintaining higher LAr purity levels in order to increase electron lifetimes, described in Section 2.2, to allow for long drifts of several meters while guaranteeing a SNR of more than 10. The long term storage of the ultrapure LAr places tight constraints on the cryostat vessel and cryogenics system in terms of their respective leak rates. In order to have drift times of a few milliseconds, oxygen equivalent impurity levels of less than 100 ppt need to be achieved and maintained during operation. As vessels of this size can not be evacuated to remove the impurities, they must be cleared away prior to cool down and filling with LAr by flushing gas argon into the detector and recirculating it multiple times until levels of $\mathcal{O}$(ppm) are reached. This so called piston purge method has been successfully applied in cryostats as large as the ICARUS T600, having a mass of 760 tons [16]. During operation, the level of impurities is maintained by recirculating the boil-off argon gas through a filter. Any new gas pumped into the detector also needs to be filtered. The evolution of O_2, N_2 and H_2O impurities inside the $3 \times 1 \times 1$ m^3 detector were studied during the piston purge before the cool down and are described in Section 4.3.

Chapter 3

Overview of the $3 \times 1 \times 1$ m^3 dual phase prototype

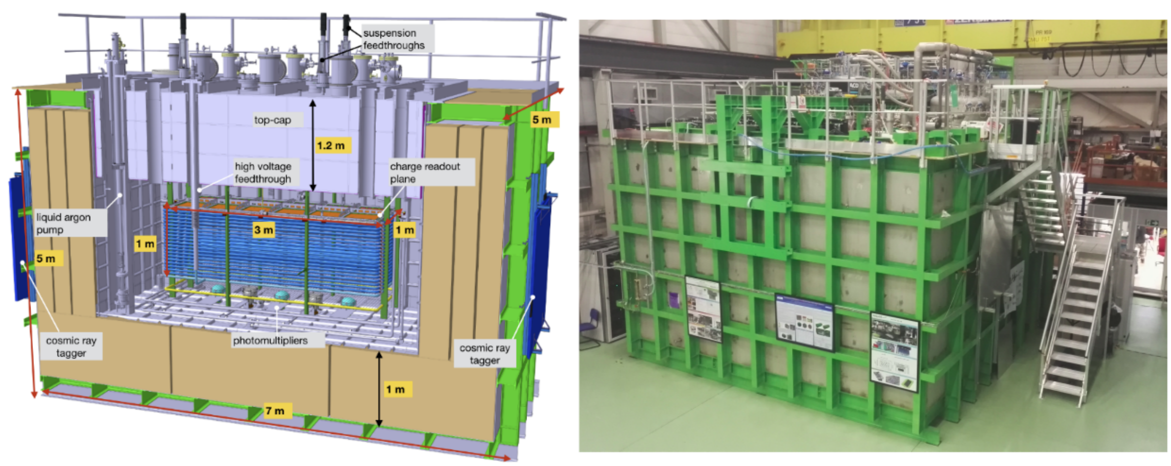

Figure 3.1: Left: Overview of the WA105 $3 \times 1 \times 1$ m^3 detector with the drift cage in the inner tank vessel, surrounded by the insulation and chimneys going through the top cap. Right: Picture of the detector inside building 182 at CERN.

The $3 \times 1 \times 1$ m^3 prototype is the first LAr dual phase LEM TPC on the scale of multiple tons, having a total LAr mass of 24 tons. The tank vessel is filled with liquid argon up to a level of about 1.5 m and a gas layer of argon extending about 0.5 m above the level of the liquid. The challenges stemming from the increased mass and CRP are described in Section 2.6. The successful operation of the detector would constitute direct evidence for the feasibility of future giant dual phase TPCs to be employed in rare event experiments, such as LBNO or Dark Matter studies. The $3 \times 1 \times 1$ m^3 is the first dual phase TPC to employ 3 m long readout strips and a significant amount of work has been invested into the minimization of crosstalk signals due to the higher capacitances between the longer strips and the performance with regard to the SNR will be an important indicator for the expediency of future giant dual phase TPC detectors. The analysis of crosstalk induced on passive strips is part of this thesis and is described in Chapter 5.

3.1 Vessel and cryostat design

The $3 \times 1 \times 1$ m^3 detector is a dual phase argon LEM TPC, consisting of the inner membrane vessel enclosing the active volume, the drift cage and the CRP, which are located in the cryostat which provides the necessary thermal insulation and is closed off on top by the top cap. The thermal insulation is passive and consists of multiple layers of permeable glass reinforced polyurethane foam, interspersed with pressure distributing layers of plywood, with a total thickness of 1 m, with glass wool placed in between the gaps. Its thickness and composition is designed to reach a residual heat input of 5 W/m^2 on the tank membrane in cold operation. This insulation space (IS) surrounds the tank vessel on all four sides and on the bottom. It is closed off on top by the top cap, which has a thickness of 1.2 m, providing thermal insulation and containing the signal, slow control and high voltage feedthrough chimneys, the cryogenic argon pump tower and the purification system. A schematic of the cryostat with the drift cage inside is shown in Figure 3.1. A detailed view of the insulation panels and the chimneys going through the top cap is given in Figure 3.2. The adopted design of the cryostat thus has the shape of an open cup with a thermally insulating top cap and the tank vessel located inside. The outer dimensions of the cryostat are 7 (length) $\times$ 5 (height) $\times$ 5 (width) m^3, enclosing the inner vessel with dimensions of 4.8 (length) $\times$ 2.4 (height) $\times$ 3 (width) m^3. A vertical uniform electric field of 0.5 kV/cm is established within the $3 \times 1 \times 1$ m^3 drift cage, using 20 field shapers spaced 5 cm apart above a metal grid cathode. The entire TPC is hung from the top cap, which is part of the tank structure, from three cables going through dedicated suspension feedthroughs.

3.1.1 Temperature and pressure sensors employed

There are a total of 153 temperature sensors for the cryostat and tank. One to measure the ambient lab temperature, 44 in the insulation space, 36 along a ribbon chain inside the purity monitoring chimney, 36 along a ribbon chain next to the field cage inside the tank, four on the membrane at the bottom of the tank, 16 on the level of the CRP, which are grouped in

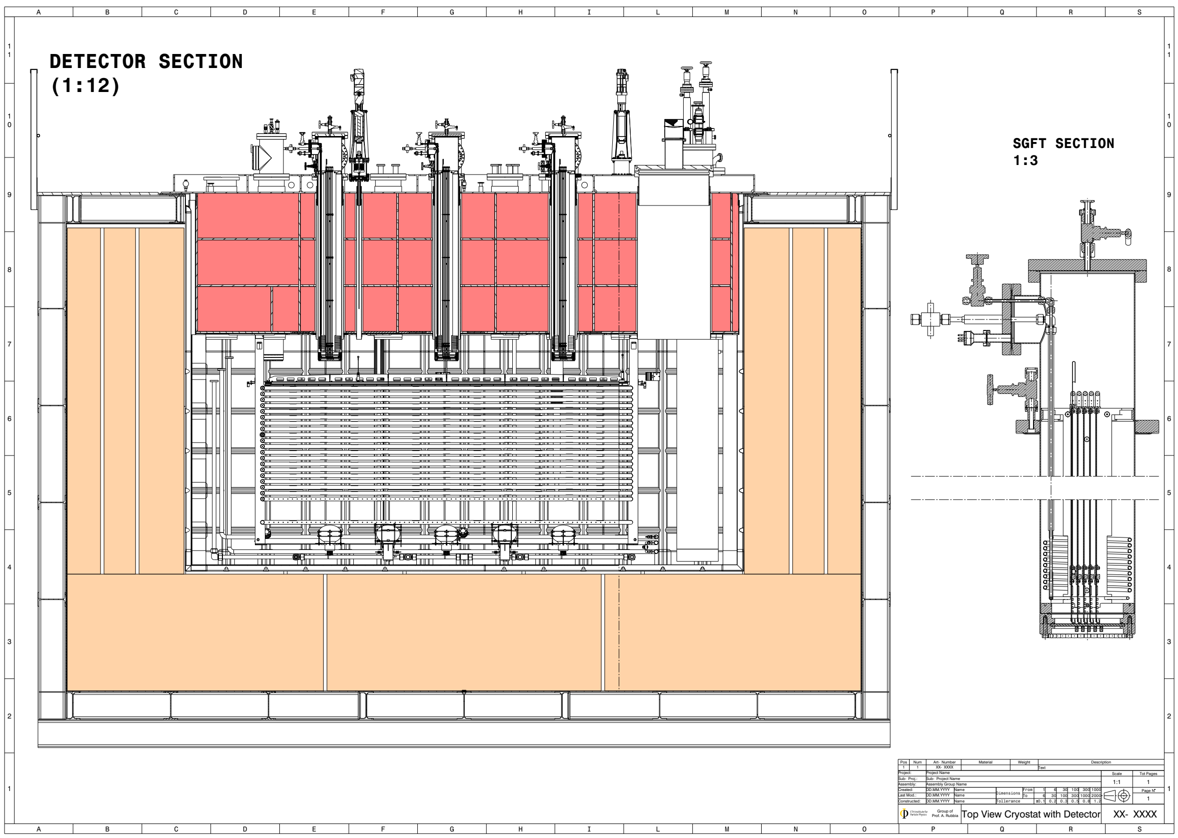

Figure 3.2: Technical drawing of the $3 \times 1 \times 1$ m^3 cryostat and SGFT chimney. The drift cage in the tank vessel is surrounded by the insulation, consisting of the insulation space on the sides and the bottom and the top cap. The high voltage, slow control and SGFT chimneys go through the insulation in the top cap.

four groups of four each, five located on heaters on the CRP to control their respective temperature, 8 thermocouple temperature sensors (2 in each SGFT chimney, one on top, one on the bottom) and 3 sensors in a drilled hole in the IS, adding to the 44 IS sensors. In addition, there are 13 pressure sensors employed inside the tank and the surrounding cryostat. One to measure the absolute pressure of the lab, two to measure the absolute pressures in the IS and top cap, two to measure the differential pressure with respect to the atmosphere of the IS, one for the differential pressure between top cap and atmosphere, one to measure the absolute pressure in the tank and two to measure the differential pressure between the tank and the top cap or the atmosphere respectively. In addition there is a differential pressure sensor for each of the four SGFT chimneys, measuring the pressure difference with respect to the atmosphere. All temperature and pressure sensors are recording data constantly and are being monitored.

The 44 temperature sensors in the IS are arranged in three layers at distances of 0.4, 0.7 and 1.0 m from the membrane of the tank. They are located in between the foam panels, forming the three layers of the insulation in the IS, show in Figure 3.2. There are 9 sensors at three different heights on the north, east and west walls as well as on the bottom and 8 on the south wall. In addition there are 3 sensors at various depths inside a drilled hole on the bottom of the south side, placed there after the first cool down of the tank (27.02.2017 - 04.03.2017) as ice formations on the outer structure were observed. These are used to monitor the potential cold spots due to air gaps found in the insulation which are believed to be the cause of the ice formations. The cool down procedure as well as the thermodynamic behavior of the cryostat during cool down is described in Chapter 4.

3.1.2 Quality of the insulation

To verify the quality of the insulation, the temperature within the IS was monitored before the cool down. A plot of the average temperature in each of the three layers over a time period of seven days is given in Figure 3.3. The temperature in the outer layer clearly shows

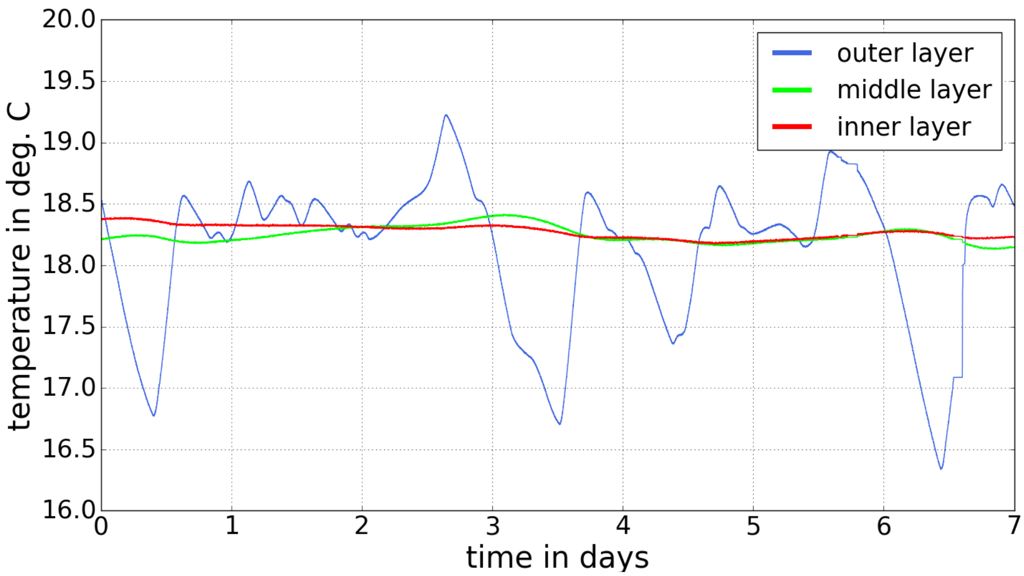

Figure 3.3: Average temperature of all sensors in the three layers of the insulation space over a time period of seven days from the 10.11.2016 until the 17.11.2016.

day/night fluctuations with an RMS value of 0.58 K over the given time period. These fluctuations become very small in size for the middle layer and even smaller for the inner layer with RMS values of 0.068 and 0.055 K, respectively. The maximum observed peak-to-peak temperature difference within the outer layer of the insulation during this time period has been 2.89 K. During this time, the maximum peak-to-peak temperature difference in the middle and inner layers was only 0.29 and 0.22 K, respectively, indicating a high quality of the thermal insulation of the IS for the tank with respect to the ambient lab temperature.

3.1.3 Cryogenics installation

The cryogenic system for the $3 \times 1 \times 1$ m^3 detector is designed to safely compensate for the boil-off argon gas by condensing it back and simultaneously purify both gas and liquid argon to a level below 100 ppt of oxygen equivalent impurities, needed to achieve electron lifetimes of more than 3 ms, as described in Section 2.2. The condenser employed in the detector has a maximum power of 10 kW, while a heat input of about 1 kW is foreseen for the $3 \times 1 \times 1$ m^3 TPC during operation, as described in Section 4.4. After recondensing the boil-off gas, it is purified using a custom made activated copper cartridge and introduced back into the tank. This method functions well in small or medium sized cryostats of multiple tons, however it is not scalable to big tanks such as the 40 kton far detector proposed for the DUNE experiment [21].

As membrane cryostats on the scale of the $3 \times 1 \times 1$ m^3 detector can not be evacuated, special systems for the purging of the tank and the subsequent cool down as well as the gas and liquid argon recirculation had to be designed. These systems suffice the purity and pressure requirements of about 100 ppt oxygen equivalent impurity levels and a tank pressure of 1000 mbar. A step-by-step operation sequence has been defined in order to safely purge and operate the cryogenic system [22]. These steps are described below in order of execution.

1. The tank is purged with gas argon, emanating from the LAr storage tank through an evaporator. This purge with gas argon lasts for at least 10 volume changes of the tank and stops once the oxygen impurities reach 10 ppm. It is referred to as the open loop purge.

2. After the open loop purge, the gas is recirculated and purified in the so called closed loop stage. During the gas recirculation, the impurities are further reduced to levels below 1 ppm. This corresponds to impurity levels below 1 ppb of the LAr, once the gas re-condenses.

3. After the open and closed loop stages, the cool down of the tank is initiated. The tank is cooled by taking the warm gas, passing it through the condenser and re-injecting the

LAr back into the tank together with gas argon through atomizing nozzles, as described in Section 4.4. During the cool down, the gas is continuously purified by both the gas purifier and a custom made activated copper cartridge, located after the condenser.

4. Once the temperature in the tank reaches 50 Kelvin above the boiling point of LAr, the tank will be filled with liquid argon passing through the activated copper cartridge.

5. After reaching the required LAr level up to the extraction grid, normal operation will begin. Here, the LAr is recirculated by a submersed centrifugal pump and the boil-off gas is re-condensed by the condenser and purified by the activated copper cartridge.

3.1.4 Gas purge of insulation

The gas above the LAr in the tank vessel will be kept at a constant pressure of about 1000 mbar in order to prevent contamination from the outside. The surrounding insulation in the IS and the top cap is closed off to the atmosphere. The top cap and IS are connected together through a plastic tube, but can be isolated from each other through a regulating valve at the connection of the tube on the top cap. Ideally, the two volumes would constitute a perfectly closed system, however, leaks in the outer cryostat structure were discovered, see section 3.1.5. In order to prevent any oxygen from liquefying (boiling point of O_2: 90 K, compared with 87 K for Ar) and thus constituting a fire hazard, the IS and top cap are being purged continuously with nitrogen (boiling point of N_2: 77 K). Nitrogen was chosen as the purging gas of the insulation instead of argon in order to guarantee that no liquefaction of gas in the insulation occurs and to be able to detect residual argon gas in case of a leak in the membrane of the tank vessel using gas analyzers. As the insulation contains leaks, it is purged continuously and kept at a constant overpressure with respect to atmospheric pressure. Nitrogen gas is pumped into the top cap from the bottom north side of the cryostat through a flow meter with a range of 0-16 ln/min (ln refers to normal liters at 0 °C and 1.013 bar). A bubbler is located at the gas input of the top cap which is filled with high-viscosity silicone bluesil fluid to avoid evaporation. As the level of liquid in the bubbler is adjustable, the overpressure with respect to the atmosphere can be set to arbitrary values between 0 and 10 mbar, provided the gas pumped in compensates for the flow out from the leaks. Placing the bubbler at the input of the gas flow guarantees that the pressure difference of the insulation with respect to the atmosphere never exceeds the pressure set on the bubbler through adjustment of the level of liquid. This pressure difference of the IS and top cap with respect to the atmosphere is given by:

$$\Delta P = \rho g \Delta h \tag{3.1}$$

where $\rho = 0.973 \text{g/cm}^3$ is the density of the silicone liquid in the bubbler, Δh is the hight difference of the liquid between the tube leading in from the outgoing connection of the top cap and surrounding liquid, and $g = 9.81$ m/s^2 is the earth's gravitational acceleration. Another advantage of having the bubbler at the input, as opposed to placing it on another port of the insulation, is the reduced flow of warm gas through the insulation thus constituting less heat input. As the top cap and IS are connected through a tube, the overpressure between these two volumes should always be equal. The schematics of the flow through the IS and the top cap as well as the bubbler are given in Figures 3.4. Since October 2016, the

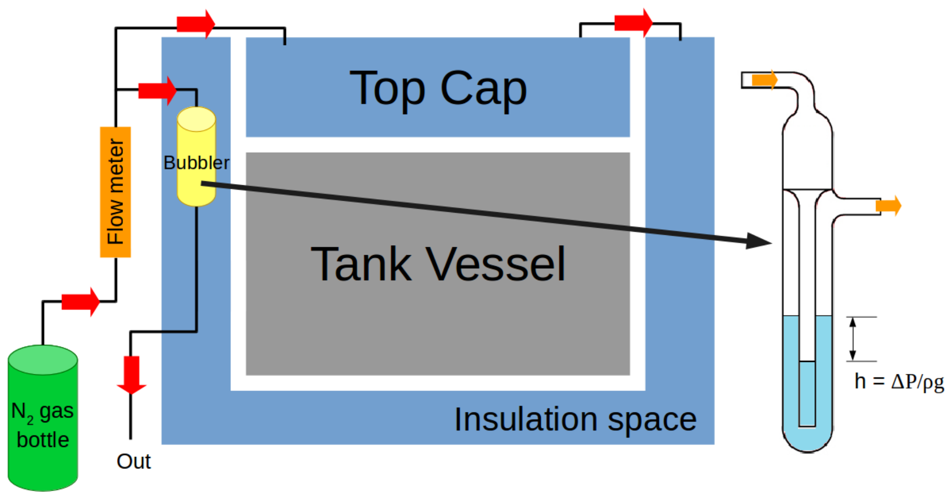

Figure 3.4: Schematic of N_2 gas flow through the insulation space and top cap. The gas is pumped in from a gas bottle through a flow meter into the top cap which is connected to the insulation space on the other side. The bubbler is located at the input.

atmospheric pressure in Geneva had minimum and maximum values of 940 and 990 mbar respectively. Assuming these are the two extrema for the pressure during operation and a tank pressure of 1000 mbar, an overpressure of the insulation of 5 mbar should always suffice the condition of $P_{tank} > P_{ins} > P_{atm}$, as the pressure of the IS and top cap should always remain below the tank pressure in order to minimize any potential contamination. This can be achieved by setting the height of the liquid above the tube leading in to $h = \frac{5 \text{ mbar}}{\rho g} = 5.2\text{cm}$.

The differential pressure between insulation and atmosphere ($P_{\text{ins}} - P_{\text{atm}}$) will generally be anti-correlated with the atmospheric pressure. As the atmospheric pressure decreases, the differential pressure will increase up to the point where it reaches the maximum pressure set by the height of the liquid in the bubbler. Then the differential pressure will just stay constant, as excess gas exits freely through the bubbler. More problematic are sudden increases in the atmospheric pressure. As it increases, the differential pressure decreases and could fall below zero if it is not compensated for by the N_2 gas flow into the insulation, set by the flow meter.

During the cool down of the detector, described in Chapter 4, the nitrogen flow rate of the flow meter was set to about 50 ln/h and the differential pressure of the insulation was found to stay constantly above zero, as can be seen in Figure 4.1. We conclude that a flow rate of 50-100 ln/h is enough to guarantee a constant overpressure in the insulation during operation and compensates for the leak rate of the outer cryostat structure as well as for sudden atmospheric pressure increases. An analysis of the pressure evolution of the tank, the IS and the top cap during the cool down is given in Section 4.1.

3.1.5 Volume and leak rate measurement of insulation

In order to measure the free volume of both the IS and the top cap, both volumes were opened to the atmosphere to set the differential pressure to zero and subsequently isolated from it and each other. The top cap was purged at a constant flow rate of 4 ln/min for 10 minutes while the pressure inside was monitored. The total volume of the top cap can thus be calculated using:

$$V_{\text{top cap}} = \frac{P_{\text{atm}} \cdot \Delta V}{\Delta P} \tag{3.2}$$

where ΔV is the volume of the gas pumped in, P_{atm} is the pressure of the atmosphere at the time and ΔP is the difference in pressure observed. The obtained free volume in the top cap is thus 5750 l. The connection between the top cap and the IS was subsequently opened while both volumes were still isolated from the atmosphere. From the pressure increase in the IS (or the pressure decrease in the top cap) and the previously obtained volume of the top cap, the volume of the IS can be calculated using:

$$V_{\text{IS}} = \frac{\Delta P_{\text{top cap}} \cdot V_{\text{top cap}}}{\Delta P_{\text{IS}}} \tag{3.3}$$

The thus obtained free volume of the IS is 4290 l, giving a total volume of the insulation of roughly 10000 l. The pressure evolution of the top cap, the IS and the atmosphere during this time is given in Figure 3.5.

In order to measure the leak rate of the IS and the top cap independently from each other, an overpressure of about 6 mbar with respect to the atmosphere has been applied to both volumes, filling them with nitrogen gas through the flow meter. Subsequently, the flow was stopped and both volumes were isolated from each other and the bubbler to measure the

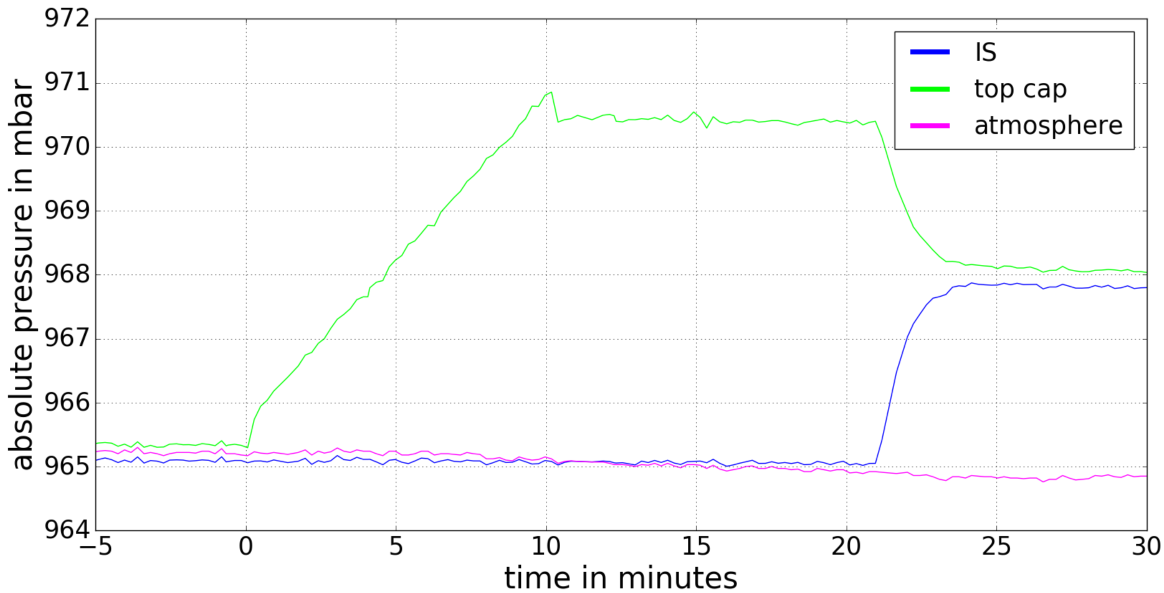

Figure 3.5: Evolution of pressures in top cap (green), IS (blue) and atmosphere (magenta) during volume measurements. The gas flow into the top cap started at zero and stopped after 10 minutes. The top cap and IS were connected after 21 minutes.

pressure decrease over time, thus enabling an accurate calculation of the leak rate. The leak rate Q_L is given by:

$$Q_L = \frac{\Delta P \cdot V}{\Delta t} \tag{3.4}$$

with ΔP being the decrease in pressure after time Δt and V is the volume of the considered vessel. Thus the initial leak rates of the IS was measured to be 3.1 $\frac{\mathrm{mbar\,l}}{\mathrm{s}}$ at an overpressure of 6 mbar with respect to the atmosphere. The leak rate of the top cap is much smaller, being less than 0.3 $\frac{\mathrm{mbar\,l}}{\mathrm{s}}$ for an overpressure of 6 mbar. The evolution of the pressures inside the top cap, the IS and the atmosphere during the leak rate measurements is given in Figure 3.6.

3.2 Overview of the charge readout plane

The $3 \times 1 \times 1$ m^3 detector employs a 3×1 m^2 CRP, consisting of the extraction grid, the LEM and the anode, and has a maximal drift length of 1 m. The anode and LEM are made up of twelve 0.5×0.5 m^2 modules, assembled in a multi-layer "sandwich", together with the extraction grid, consisting thin metal wires and guaranteeing the efficient extraction of the electrons from the liquid using an electric field of about 2 kV/cm, as described in Section 2.3.2. The extraction grid is located 5 mm below the LAr surface and is made up of two sets

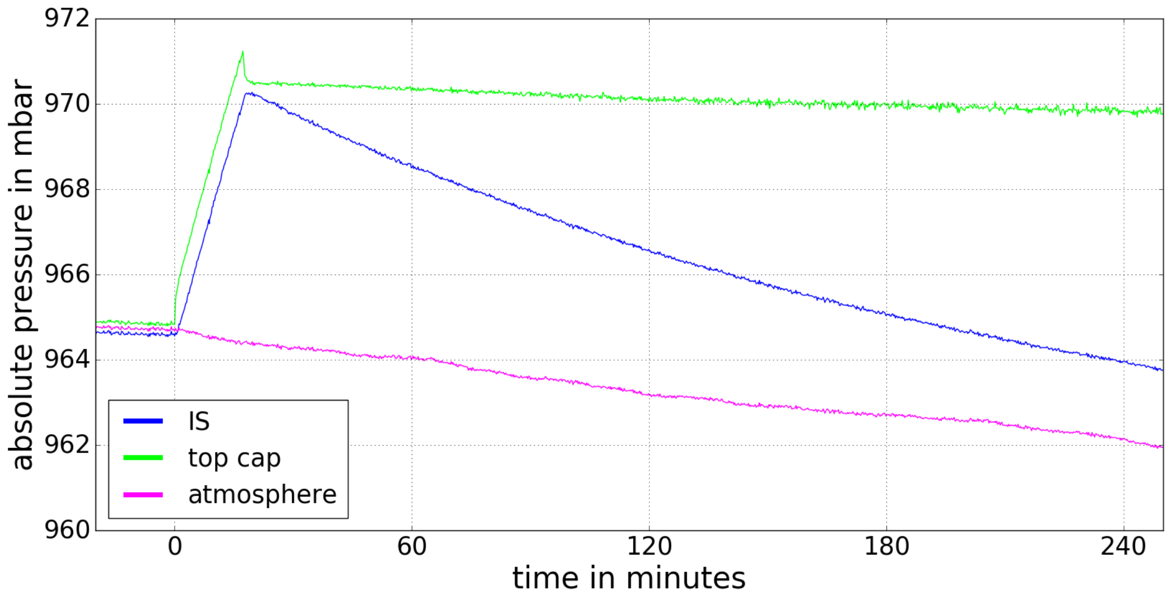

Figure 3.6: Evolution of pressures in top cap (green), IS (blue) and atmosphere (magenta) during leak rate measurements. The gas flow into the insulation started at zero and stopped after 17 minutes after reaching a differential pressure of 6 mbar. Subsequently, the top cap and IS were disconnected from each other and left isolated for 4 hours.

of 100 μm diameter wires, matching the pitch of the anode strips of 3.125 mm. The wires are tensed across the 3×1 m^2 area of the CRP.

The key concept of the dual phase TPC relies on the extraction of the electrons from the liquid to the gas phase where they can be amplified in the LEMs. The LEMs functin by triggering Townsend avalanches due to the high electric field regions of about 30 kV/cm inside their holes. Once amplified in the LEM, the electrons are then collected and recorded on a two-dimensional and segmented anode. Both the anode and LEM modules are produced as rather standard PCBs that can be easily mass-produced at low costs. A picture of the CRP with the LEM and anode is shown in Figure 3.7. The anode consists of two sets of parallel strips (views) that provide the 2D x and y coordinates of the events, as described in Section 2.3.2, designed to have equal charge sharing between the two views and a low capacitance of each strip to the rest of the anode. The two sets of strips are composed of individual pixels, consisting of strip segments, with a pitch of 3.125 mm. The strip segments are connected through wires in a layer below the collection plane, as shown in Figure 5.8.

The charge collected on the strips is read out at the end using specially designed low-

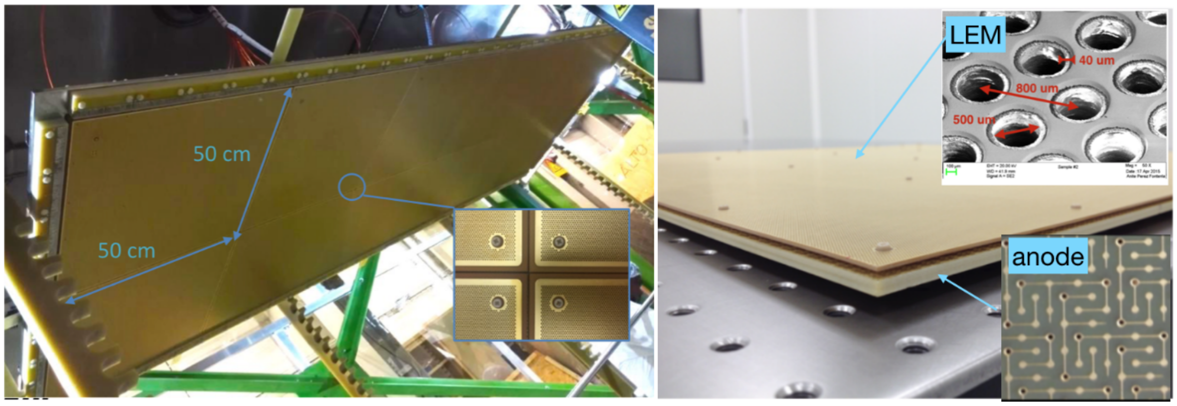

Figure 3.7: Left: Bottom view of the CRP showing the fully active 3×1 m^2 amplification area. Right: An individual LEM and anode sandwich with zooms on their surfaces.

impedance charge-sensitive preamplifiers. The readout electronics consist of the preamplifier which has an impedance to ground of a few Ohm and a feedback capacitor across the preamp. In order to maximize the amplification of the signal, the feedback capacitor should be as small as possible, it is 1 pF in this case. The charges are thus drained towards the ground potential of the preamp, where the signal is amplified. The preamps are located in the SGFT chimneys, which are described in Section 3.3. After the amplification stage, the signals are digitized and recorded in accessible crates, located on top of the top cap.

One of the goals of the $3 \times 1 \times 1$ m^3 detector is to demonstrate that a uniform gain and detector response of the readout electronics can be achieved at the multi-square meter scale. Thus the design and the quality control of the extraction grid, the LEM and the anodes are crucial aspects in terms of the performance of the detector. These designs are the product of many years of research and development, including many prototypes employed on smaller scale LAr TPCs, such as the 3 liter dual phase TPC [14]. These research efforts included testing the performance of various strip layouts and patterns on the anode [12] as well as LEMs of varying hole sizes, hole pitches, rim sizes and thicknesses [14]. The LEM and anode employed in the $3 \times 1 \times 1$ m^3 detector are the result of these investigations, with the pattern on the anode optimized to ensure exact charge sharing between the two views and the best resolution in terms the dE/dx information of the ionizing particles, and the type of LEM chosen to provide the most stable gain in dual phase conditions. Thus, we are confident, that the components of the CRP match the required performance in terms of gain stability, charge uniformity and resolution.

The mechanical tolerances in cryogenic conditions of the CRP frame were verified by dipping it multiple times into open liquid nitrogen baths and using precise survey methods such as photogrammetry [23].

3.3 Signal feedthroughs and charge readout principle

The signal feedthrough chimneys, slow control feedthrough chimneys (SCFTs) and the high voltage connection chimney go through the top cap and enclose the wires for the CRP signals, the slow control connections and the high voltage cables respectively. The volumes of these chimneys are isolated from the tank and the top cap, the wires pass through PCB boards at the two flanges of the chimneys which provide a vacuum-tight seal.

Similar to the insulation, in order to prevent any oxygen from liquefying (boiling point of O_2: 90 K, compared with 87 K for Ar) and thus constituting a fire hazard, the chimneys have been purged with nitrogen (boiling point of N_2: 77 K). The pressure in the SGFTs has been monitored during the cool down of the detector and the evolution is described in Section 4.2.

Each SGFT chimney in the $3 \times 1 \times 1$ m^3 detector reads out 320 channels and consists of a 2 meter long stainless steel cylinder, sealed on both ends by circular multilayer PCBs with connectors welded on both sides. The PCB connections were designed to provide ultra-high vacuum leak-tightness, tested before the cool down was initiated and described in Section 4.2. The bottom PCB serves as interface between the connection to the anode and the five amplifier boards located inside the chimney, as described in Section 3.4. Each board is guided from the top thanks to specially designed FR4 blades. A complete insertion of the blade guaranties that the board is electrically connected to the bottom PCB. The top PCB then serves as interface between the amplified signals and the digital electronics located in accessible crates on top of the cryostat. A technical drawing of the SGFTs with the blades inserted can be found on the right side of Figure 3.2.

The feedthroughs are crucial components of the detector and serve as the interface for signal, high voltage and slow control sensors between the inside of the detector and the experimental acquisition. They are all situated on the top cap and have to penetrate the 1.2 meter thick insulation to reach the various parts of the detector. Figure 3.8 shows a single chimney before it was inserted into the top cap as well as the PCB connections on the top and bottom.

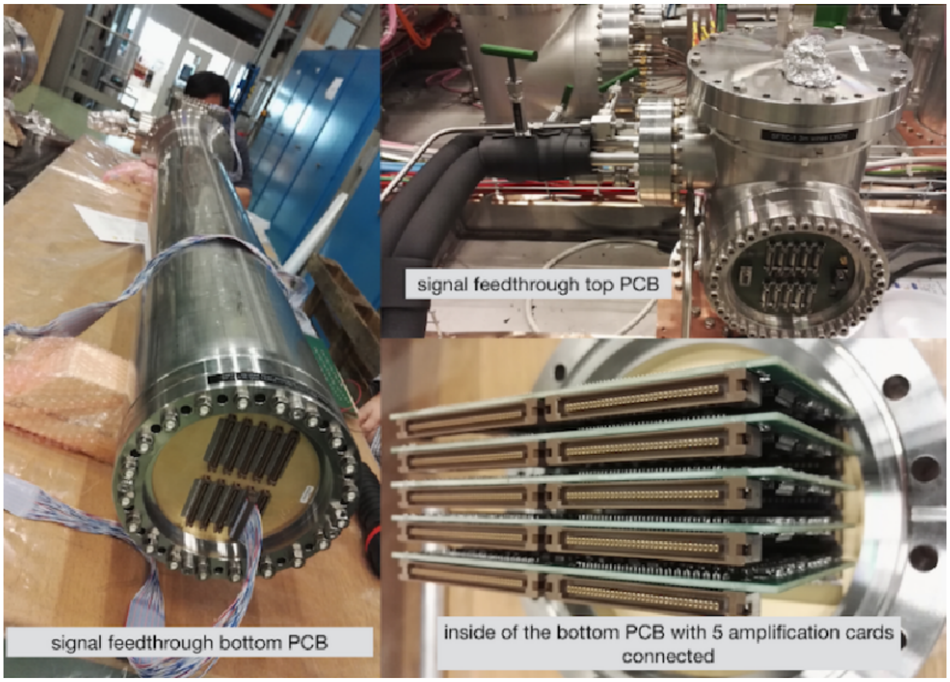

Figure 3.8: Left: Signal feedthrough chimney before installation on top cap with view of bottom PCB. Upper Right: SGFT installed on top cap with view of upper PCB. Lower Right: the five amplification cards on the bottom PCB of the chimney for reading out the signals on 320 strips.

The installed feedthroughs are based on innovative concepts and will be tested during operation. An excellent SNR is imperative to reach the performance required for rare event studies, such as neutrino physics. The SGFT chimneys allow to place the amplification stage close to the anodes, thus also profiting from the cold environment, while still being able to extract the boards, located on blades that slide out vertically, for maintenance without accessing the tank vessel. In this context, the innovative design of the installed feedthroughs will be tested during operation and will be either copied or scaled up for future larger detectors. Strict requirements placed on the chimney's vacuum tightness, high voltage breakdown limits and cryogenic compatibility, meant that they had to be custom designed in close collaboration with the industry.

3.4 Mapping of channels

There are 1280 channels in total, split into the two views, called view 0 and 1. The 3×1 m^2 CRP employs 320 3 meter long strips constituting view 0 and 960 1 meter long strips constituting view 1. The signals of the channels on the anode are read out inside the signal feedthrough chimneys, which are described in Section 3.3. There are four SGFT chimneys, labeled SGFT1, SGFT2, SGFT3 and SGFT4. Each chimney contains the frontend electronics, that is the preamplifiers, for 320 channels. All 320 channels of view 0 lead to the preamps in SGFT1; the 960 channels of view 1 are split between SGFT2, SGFT3 and SGFT4. Each chimney accommodates five amplifier boards, located on five specially designed FR4 blades, which can be vertically inserted into the chimneys from the top. After being amplified on the boards inside the chimneys, the channel signals are passed through the top PCB to the digital electronics, located on top of the cryostat.

Each of the five amplifier cards in each chimney thus reads 64 channels and is divided into two connectors with 32 channels each. Each connector spans a group of 32 neighboring channels on the anode, of whom there are 10 in view 0 and 30 in view 1. The anode consists of twelve 0.5×0.5 m^2 modules, with each module having 160 channel strips in each view. Each of the two connectors within a card read a group of 32 channels from a different module. Figure 3.9 shows the mapping of each group of 32 channels to the connectors on the blades in the four chimneys.

3.5 Detector response and charge yield

MIPs are particles with a mean energy loss rate at the minimum of the stopping power for a given medium. This energy loss rate is 210 keV/mm for a MIP in LAr. The average ionization energy of liquid argon is 23.6 eV. Thus about 8900 electrons/mm are obtained immediately after a MIP passes though the detector. A fraction of the initially created electrons will recombine immediately with the ions, yielding a charge of $Q_r = R \cdot Q_0$, where Q_0 is the initial charge of the electrons, Q_r is the remaining charge after recombination and R is the recombination factor. For a drift field of 500 V/cm, about 70 % of the initially created charges remain after recombination, according to the experimentally proven Birk's law [24]. These 6230 electrons/mm are free to drift to the top of the liquid and be extracted into the gas phase. Further attenuation occurs, according to the drift length and the impurities present in the LAr, as described in Section 2.2. Prior to their collection on the anode strips, the electrons are multiplied in the LEMs with an assumed effective gain of 20, that is a gain of 10 per view. A stable effective gain of 20 was previously obtained for a 3 liter dual phase TPC detector [12]. Subsequently, the electrons are collected on the strips of the anode in the two views, with a readout pitch of 3.125 mm. The number of electrons is split equally between the two views, as the design of the anode guarantees equal charge sharing between them. The total charge collected on one strip from a MIP track being in the horizontal plane

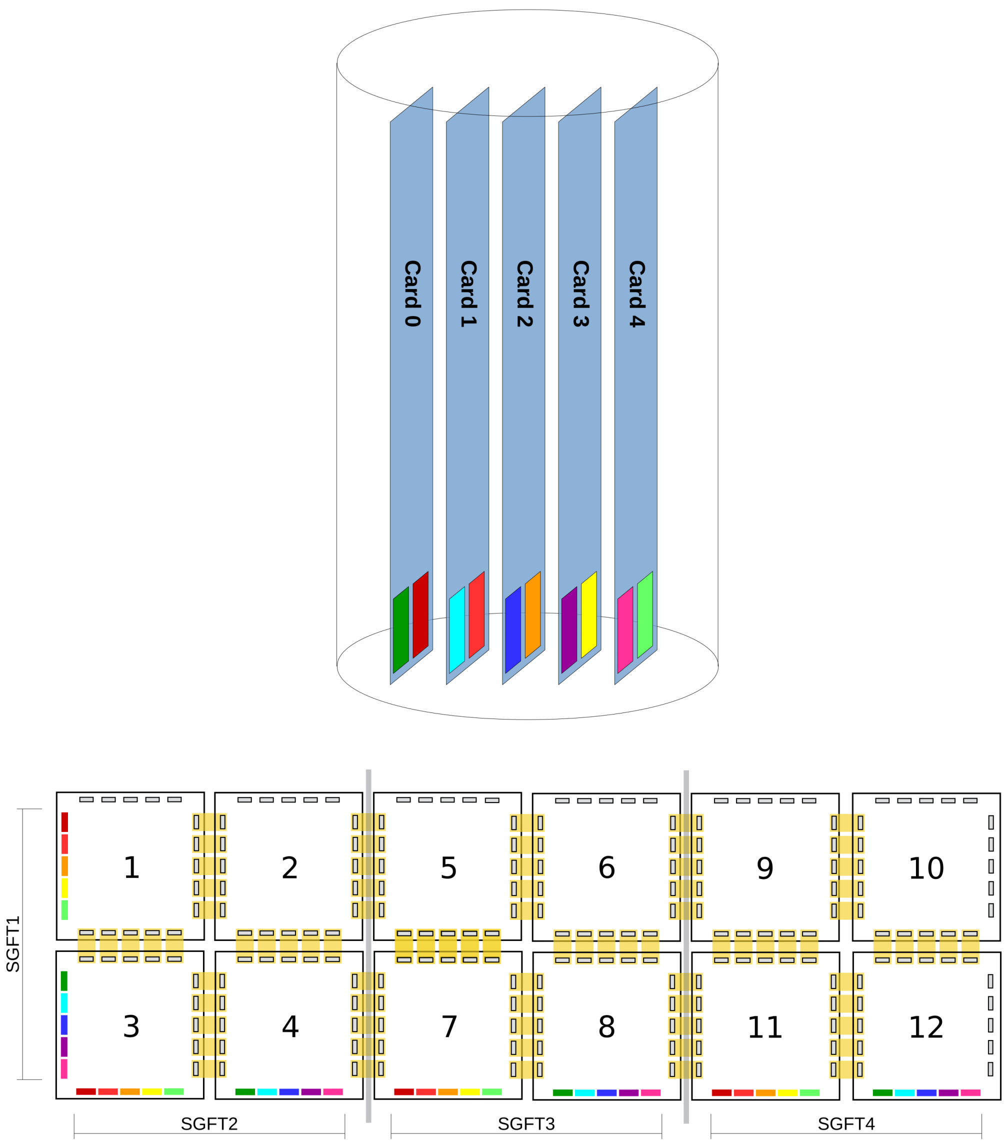

Figure 3.9: Mapping of groups of 32 channels on the anode to the connectors on the cards in the chimneys, indicated by the colors. Each chimney reads out 320 channels, with each of the five cards reading 64 channels split into two connectors, each reading 32 channels from different modules.

and perpendicular to the strip, is given by:

$$Q = \frac{\frac{dE}{dx}}{W} \cdot R \cdot (1 - A) \cdot G_{eff} \cdot p/2 \tag{3.5}$$

where $\frac{dE}{dx}$ is the energy loss rate, W is the ionization energy of the medium, R is the recombination factor, A is the attenuation due to the finite electron lifetime over the drift length due to impurities, described in Section 2.2, G_{eff} is the effective gain, as described in Section 2.3.2, and p is the pitch of the strips. The factor of 1/2 accounts for the charge splitting between the two views. Table 3.1 shows the number of electrons collected on a strip for a MIP track in the horizontal plane and perpendicular to the strip, for an effective gain of 1 and 20, and various oxygen equivalent impurity levels for a drift field of 0.5 kV/cm. Also shown is the

	infinite e^- lifetime	with 1 m drift and 100 ppt O_2 equivalent impurities	with 1 m drift and 500 ppt O_2 equivalent impurities
proportion of remaining electrons $(1-A)$ due to finite lifetime	100 %	81.7 %	36.4 %
number of e^- (charge) collected on one anode strip, $G_{eff}=1$	9730 (1.56 fC)	7950 (1.27 fC)	3540 (0.57 fC)
SNR with an assumed noise RMS of 1500 e^-, $G_{eff}=1$	6	5	2
expected waveform amplitude, $G_{eff}=1$	10 ADC	8 ADC	4 ADC
number of e^- (charge) collected on one anode strip, $G_{eff}=20$	194600 (31.2 fC)	159000 (25.4 fC)	70800 (11.4 fC)
SNR with an assumed noise RMS of 1500 e^-, $G_{eff}=20$	130	106	47
expected waveform amplitude, $G_{eff}=20$	208 ADC	169 ADC	76 ADC

Table 3.1: Attenuation for oxygen equivalent impurity levels of 100 and 500 ppt for a drift length of 1m and a drift field of 0.5 kV/cm. Also given is the number of electrons collected on one strip for a MIP track in the horizontal plane, perpendicular to the strip for an effective gain of 1 and 20 and various impurity levels, as well as the SNR for a RMS of the noise of 1500 electrons and expected waveform amplitude with a sensitivity of the electronics of 0.15 fC/ADC.

expected amplitude of the waveform based on the sensitivity of the readout electronics of 0.15 fC per analog-to-digital converter (ADC) count, for the described MIP track. The SNR is also shown for an RMS of the noise of 1500 electrons, with the target of having a noise level below that for the strips of the detector. The signal-to-noise ratio is simply defined as the ratio between the number of electrons collected on one strip and the RMS of the noise. The level of noise is highly dependent on the characteristic capacitance to ground of the readout strips and on the front end electronics, namely the preamplifiers. A full characterization of the capacitances of one strip to other components of the anode, as well as signals induced through capacitive couplings are given in Sections 5.4 and 5.3 respectively.

Chapter 4

Thermodynamic behavior and pressure evolution during cool down

Before the first cool down of the detector was initiated, the tank was purged first in open and then in closed loop. During the open loop purge, argon gas coming from evaporated liquid argon from the LAr tank was introduced to the cryostat through 12 holes which are uniformly distributed at the bottom of the tank through a manifold of four pipes with three holes each. The exhaust gas is vented directly to the outside through one-way valves, preventing back flow. The impurity levels are constantly monitored with the help of three trace analyzers for nitrogen, oxygen and moisture. In the subsequent closed loop stage, the gas argon inside the tank is recirculated and purified using a large capacity double diaphragm pump at a speed of 200 l/min. The commercial gas purifier removes impurities such as H_2O, O_2, CO, CO_2 and H_2 but has little effect on the nitrogen impurities. From time to time, pure argon gas is injected into the tank through a gas line to dilute the impurities further. The evolution of impurities during the gas purge and cool down of the detector is described in Section 4.3.

The first cool down of the detector was initiated on the 27.02.2017 at 09:00. A mixture of warm gas argon and LAr was injected through special gas atomizing nozzles at the bottom of the detector as a spray with the LAr evaporating due to the warm gas and thus providing the cooling power. Using this method, uniform and steady cooling of the tank volume is achieved. A more detailed description of the cool down procedure is given in Section 4.4. After about four days of cooling down, ice formations were observed on the south-east corner of the outer structure of the cryostat and the tank was warmed up again on the morning of the 04.03.2017 and the following days. An investigation revealed, that the ice formations were caused by air gaps within the fiberglass insulation panels in the IS which led to local cold spots. Holes were drilled in the outer steel structure of the IS to fill the volumes of missing fiberglass with expandable polyurethane foam in order to guarantee a uniform thermal insulation.

4.1 Pressure evolution in tank and insulation

During the first cool down, the insulation was purged with nitrogen as described in Section 3.1.4. The flow meter was set to a constant flow rate of about 50 ln/h for the entire cool down. Figure 4.1 shows the evolution of the tank pressure, the pressure in the insulation and the atmospheric pressure over a time period of two days during the cool down. The pressure

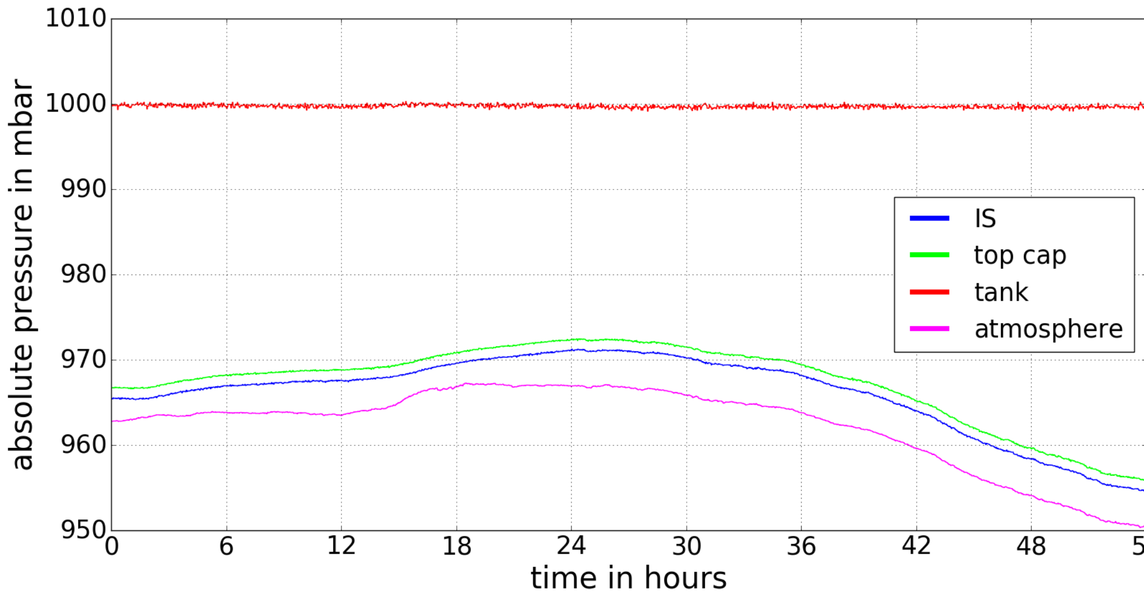

Figure 4.1: Absolute pressures of tank, insulation and atmosphere during the first cool down (27.02.2017 - 04.03.2017). The flow meter was set to a constant flow rate of 50 ln/h during this time.

in the tank has been kept very constant at 1000 mbar, with a RMS value of 0.19 mbar and was unaffected by pressure fluctuations in the atmosphere. The pressure in the insulation has been constantly kept above the atmospheric one, with the differential pressure kept positive between 2.0 and 4.6 mbar.

4.2 Pressure in chimneys

The SGFT and the High Voltage connection chimneys both have isolated volumes of gas which are in thermal contact with the tank through the bottom flanges. Hence there is an

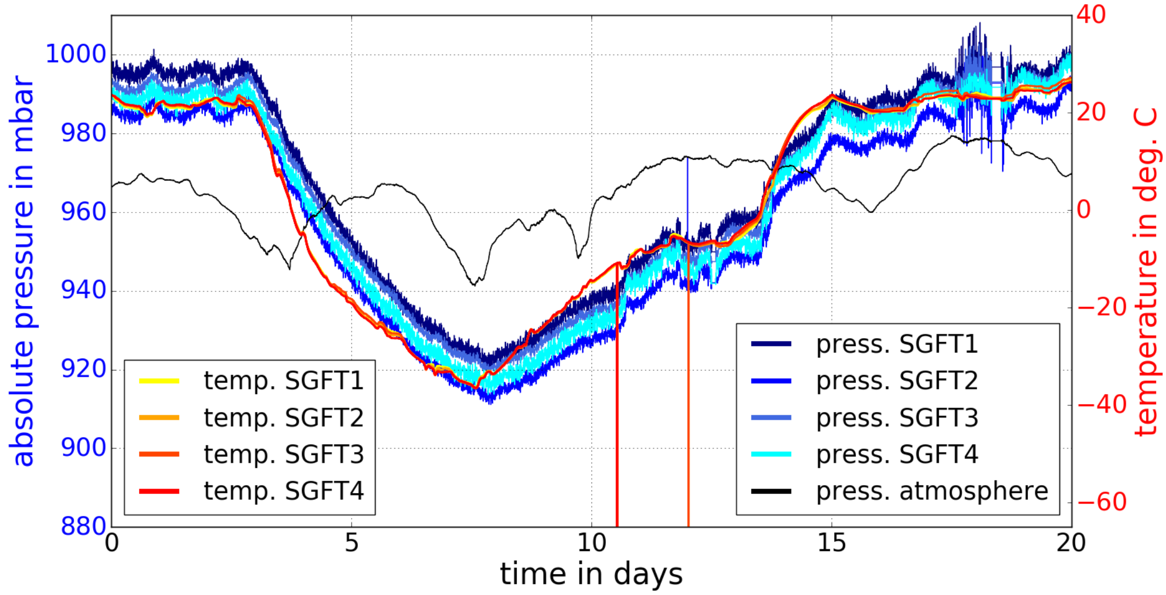

Figure 4.2: Pressures and temperatures inside SGFT chimneys during cool down and warm up of detector as well as the atmospheric pressure. The axis for the pressures is on the left (blue), the one for the temperatures on the right (red).

additional risk of having oxygen liquefy in these volumes. The inner volumes of the chimneys have been purged with nitrogen to avoid this risk. The SGFT chimneys have been checked for leaks by evacuating them using a primary vacuum pump to a level below 0.1 mbar and leaving the vacuum for over 30 hours. After tightening all connections on the flange and applying vacuum grease the pressure increase in the evacuated chimneys was below the range of the vacuum sensor used, thus indicating a very small leak rate.

All SGFT chimneys have been filled with nitrogen to a pressure of about 20-30 mbar above atmospheric. This ensures that the pressure is less than the tank pressure during operation and mostly above atmospheric pressure, satisfying the same condition as the insulation of $P_{tank} > P_{SGFT} > P_{atm}$. As the volume of the SGFT chimneys is isolated and in contact with the tank, the nitrogen inside the chimneys cools down with the cool down of the tank. This leads to a decrease in pressure according to:

$$\Delta P = \frac{nR\Delta T}{V} \tag{4.1}$$

Figure 4.2 shows a plot of the differential pressures in the SGFTs during the cool down (initiated on the 27.02.2017) and warm up (initiated on the 04.03.2017) of the detector, the temperature inside, taken from thermocouple sensors, and the atmospheric pressure. The pressure inside the chimneys is strongly correlated to the temperature, according to Equation 4.1. However, the changes in atmospheric pressure have little to no effect on the pressure inside the chimneys, confirming a very small leak rate of less than 7.9×10^{-3} mbar l/s, calculated using Equation 3.4 using the data from the vacuum test. After the warm up of the detector, the SGFT chimneys have been connected to a gas bottle of nitrogen through a pressure reducer, which consists of a one way valve and will leave the pressure unchanged until the pressure difference drops below 20 mbar. Thus Nitrogen gas will be added automatically during the next cool down, ensuring a constant overpressure in the chimneys with respect to the atmosphere at all times through an automated system.

4.3 Evolution of impurities during gas purge and cool down

The tank was purged with argon gas before the cool down in order to minimize the impurities present to guarantee a long electron lifetime. The purge consists of two main phases, the first one being the open loop purge, followed by the closed loop stage, as described in Section 3.1.3. The open loop purge was initiated on the 24.01.2017. The initial impurity level of oxygen was 6 % instead of the ∼20 % in the atmosphere due to previous purges, used to test and debug the system. Gas argon was introduced into the tank from evaporating LAr from the LAr tank through 12 uniformly distributed holes of a manifold at the bottom of the detector, shown in Figure 4.3. The excess gas was vented directly to the outside. Three trace analyzers for oxygen, nitrogen and moisture were continuously monitoring the impurity levels during the open and closed loop stages and during cool down. The impurity levels dropped from 100, 100 and 50 ppm (the upper measurable ranges of the trace analyzers) to 0.4, 1.7 and 43 ppm for oxygen, nitrogen and moisture respectively. The high level of moisture is mainly due to out-gassing from the detector components inside the cryostat. The low oxygen and nitrogen levels indicate good tightness of the tank.

During the next phase, the closed loop stage, the gas argon inside the tank was recirculated and purified using a large capacity double diaphragm pump. The purifier removes oxygen and moisture using copper pellets to remove oxygen in the reaction $O_2 + 2Cu \rightarrow 2CuO$ and a molecular sieve to remove the water by physical absorption. The purifier has little effect on the nitrogen impurities. From time to time, pure argon gas was injected into the tank to dilute the impurities. During the closed loop stage, the impurities for oxygen, nitrogen and moisture reached 0.2, 3.5 and 25 ppm respectively. A plot of the evolution of impurity levels is shown in Figure 4.4.

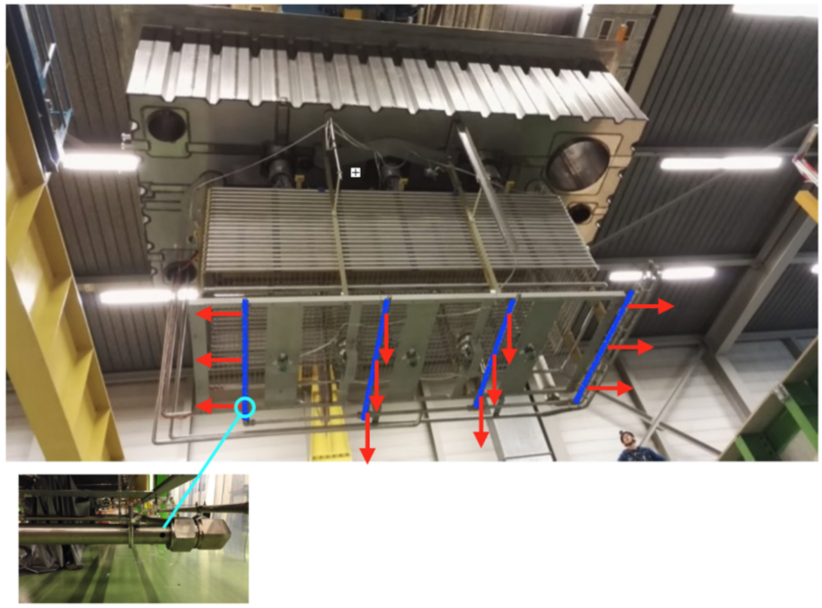

Figure 4.3: Picture of the detector during assembly with the manifold located at the bottom of the drift cage. The direction of the gas argon purge holes is indicated by the red arrows.

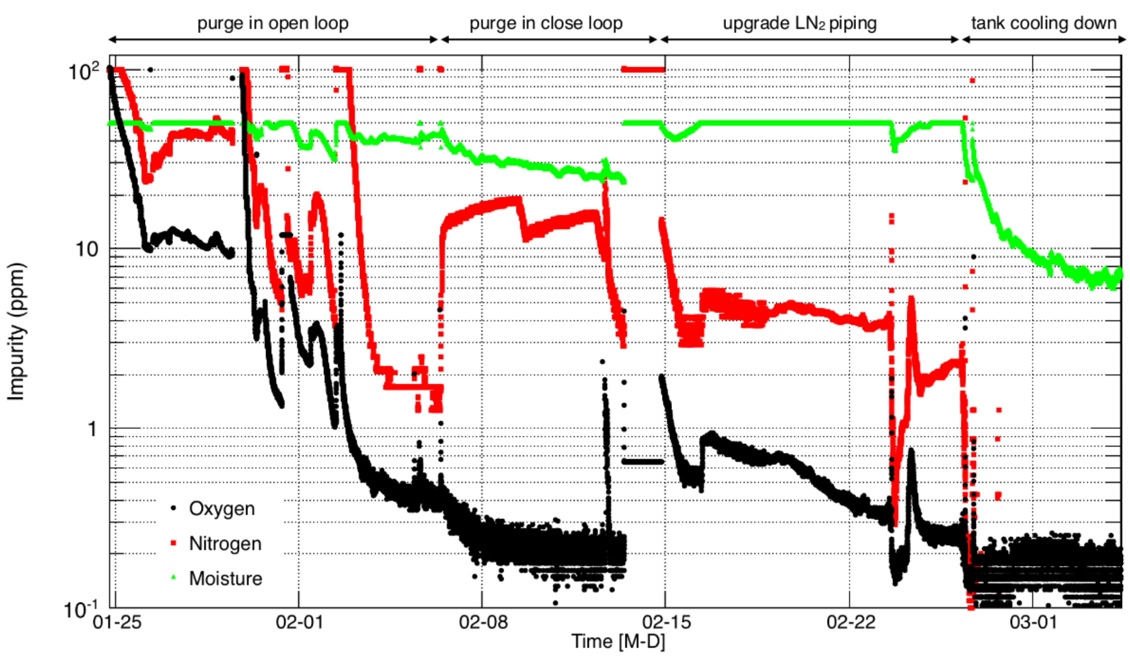

Figure 4.4: Evolution of the oxygen, nitrogen and moisture impurities during the closed and open loop purges and the cool down of the detector.

4.4 Heat input during cool down and operation

The cool down of the cryostat began on February 27th at an initial rate of about 2 Kelvin per hour. Figure 4.5 shows the evolution of the temperature gradient in gas recorded by a ribbon chain of 36 sensors placed along the drift cage. The 36 probes, which are spaced 4

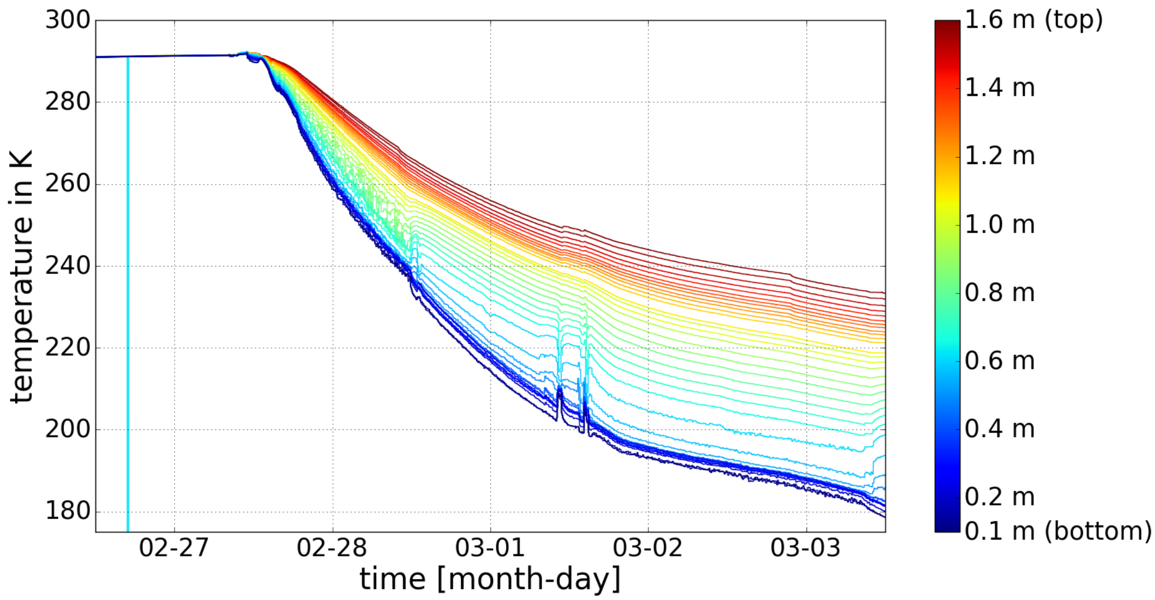

Figure 4.5: Evolution of the gas temperature inside the tank during the cooling down process. The probes are fixed along the drift cage; the bottom-most probe is located about 10 cm from the membrane floor and the top one is situated just above the CRP.

cm apart, record the gradient over a distance of 1.5 meters from 10 cm above the bottom of the tank up to the CRP. Cool down of the detector is achieved by pumping in liquid and gas argon through atomizing nozzles, located at the bottom of the cryostat. The gas which is at room temperature mixes with the 87 K cold LAr as they are injected through four gas atomizing nozzles with flow rates of 500 l/min and 21.1 l/h respectively. A great advantage of this method is that uniform and steady cooling of the detector is achieved by generating a spray of liquid argon. This method was successfully employed for previous cryostats, such as a 35 ton single phase TPC at FNAL [25]. During the cool down, sufficient cooling power needs to be provided to compensate for the total heat input from the detector feedthroughs, cables and cryostat membrane. Additional heat is introduced through the injection of the warm argon gas through the atomizing nozzles. These heat inputs need to be compensated for by the cooling power of the injected LAr including its evaporation.

During operation, the heat input from these components remains in addition to the heat inputs of the LAr pump and the electronics. However, the heat input from the injection of the warm gas is no longer present. The cooling power is provided by a condensator with a maximum cooling power of 10 kW. By design, the membrane of the tank guaranties a uniform 5 W/m^2 heat transfer at LAr temperature. The values of the estimated heat inputs during cool down and operation are given in Table 4.1.

Source	**Heat input during cool down**	**Heat input during operation at 87 K**
Membrane surface	$0.972\,\frac{\text{W}}{\text{K}} \times \Delta T$	200 W
Chimneys	$1.94\,\frac{\text{W}}{\text{K}} \times \Delta T$	400 W
Top cap	$0.29\,\frac{\text{W}}{\text{K}} \times \Delta T$	60 W
Wires	$0.028\,\frac{\text{W}}{\text{K}} \times \Delta T$	5.8 W
Electronics	0 W	23 W
Pump	0 W	300 W
Warm gas pumped in	$7.1\,\frac{\text{W}}{\text{K}} \times \Delta T$	0 W
Evaporation of liquid	- 1344 W	0 W
Warming up of evaporated liquid	$4.28\,\frac{\text{W}}{\text{K}} \times (\Delta T - 206\,\text{K})$	0 W
Total	$14.61\,\frac{\text{W}}{\text{K}} \times \Delta T - 2226\,\text{W}$	989 W

Table 4.1: Summary of all sources contributing to the heat input and cooling during cool down and operation. $\Delta T = T_{lab} - T_{tank}$, where $T_{lab} = 293$ K.

From these values a total heat transfer of $\dot{Q} = -2226\,\text{W} + 14.61\,\text{W/K} \times \Delta T$ is obtained during cool down, where $\Delta T = T_{lab} - T_{tank}$ is the temperature difference of the tank with respect to the ambient lab temperature of 20 °C. Assuming that the internal energy of the gas is proportional to its temperature, we obtain the following differential equation:

$$-\frac{d\Delta T}{dt} \propto -a + b \times \Delta T \tag{4.2}$$

with $a = 2226$ W and $b = 14.61$ W/K calculated from the values in Table 4.1. The solution to this equation is a bounded exponential function:

$$\Delta T(t) = \frac{a}{b}\left(1 - \exp\left[-\frac{b}{c}t\right]\right) \tag{4.3}$$

with c being the proportionality constant in Equation 4.2 and the initial condition $\Delta T(0) = 0$.

This calculation is verified experimentally as shown in Figure 4.6: a plot of the temperature difference between the average gas temperature near the CRP and the lab temperature during the cool down is fitted with an exponential function. The fit was obtained using a least squares algorithm and constricting the values of the fit parameter a to below 2500 W. The obtained fit parameters are $a = 2265$ W and $b = 33.17$ W/K, to be compared with the values in Table 4.1. The difference between the fitted value for b and the estimated one, can be

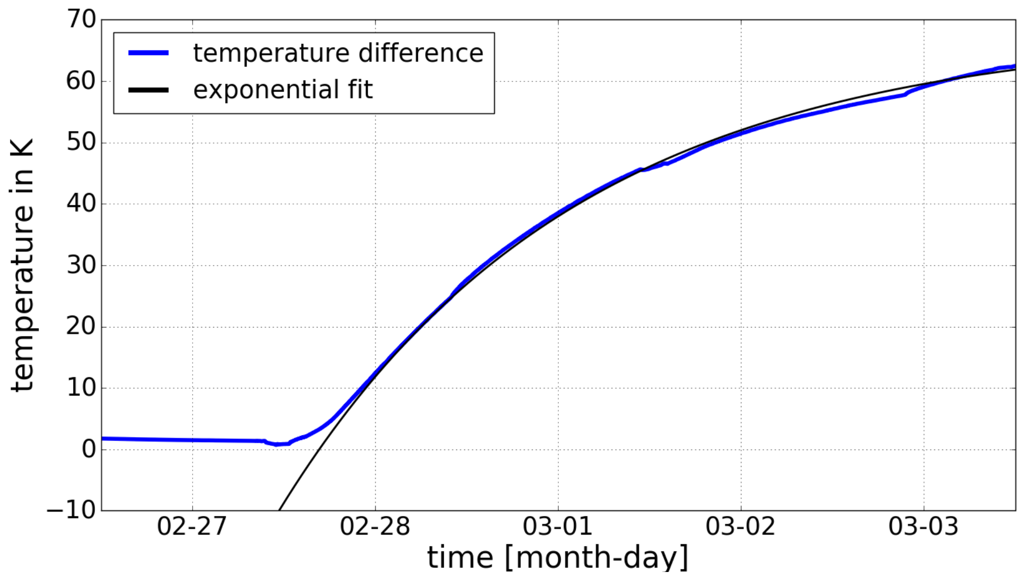

Figure 4.6: In blue, evolution of recorded temperature differences between the CRP and the lab during the cool down process; in black, exponential fit obtained from a least squares optimization procedure.

explained by the air gaps found in the insulation that led to local cold spots on the outer cryostat structure and gives an estimation of the heat input resulting from these defects in the insulation material.

The evolution of the measured temperatures on the level of the CRP, obtained from the 16 temperature sensors, arranged in four groups of four each, is given in Figure 4.7. The temperatures evolution on the CRP was very uniform during the cool down process with temperature variations of less than 5 K between the sensors. The initial cool down rate was about 2 K/h and decreased exponentially. A temperature of about 230 K was reached until ice formations were observed on the outer structure, resulting from air gaps. Assuming the temperature decrease is an exponential function as described previously, the minimum temperature that could have been reached with the described setup would have been 225 K, compared to the required temperature of 87 K (temperature of LAr).

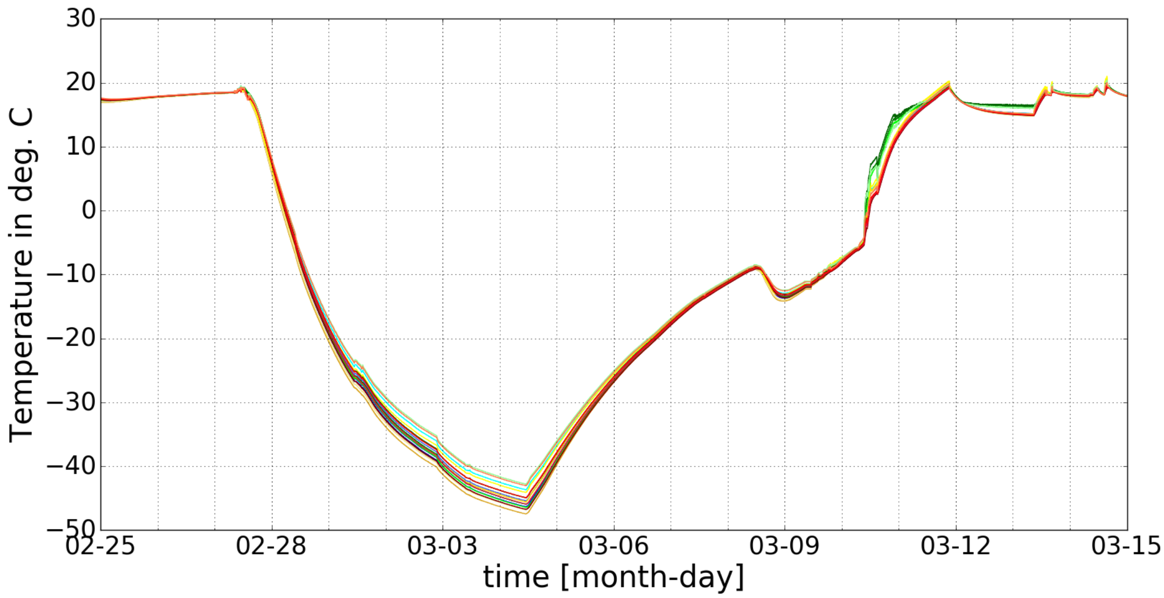

Figure 4.7: Evolution of the temperature on the CRP during cool down and subsequent warm up. 16 temperature sensors in total, grouped in 4 groups of 4 each. The differences in temperature between sensors are less than 5 K.

In addition, the temperature was monitored along a ribbon chain of 36 temperature sensors in the purity monitoring chimney during the cool down. A plot of these temperatures is given in Figure 4.8. The top flange, which effectively remained at room temperature shows clear day night fluctuations, with an RMS value of 1.3 K. With increasing distance from the top flange, these fluctuations become less, with the sensor closest to the bottom flange not showing any discernible fluctuations over the period of the cool down. The minimum temperature reached by the bottom sensor was 245 K before the warm up started, compared with 228 K on the CRP and 173 K on the bottom sensor of the ribbon chain along the drift cage.

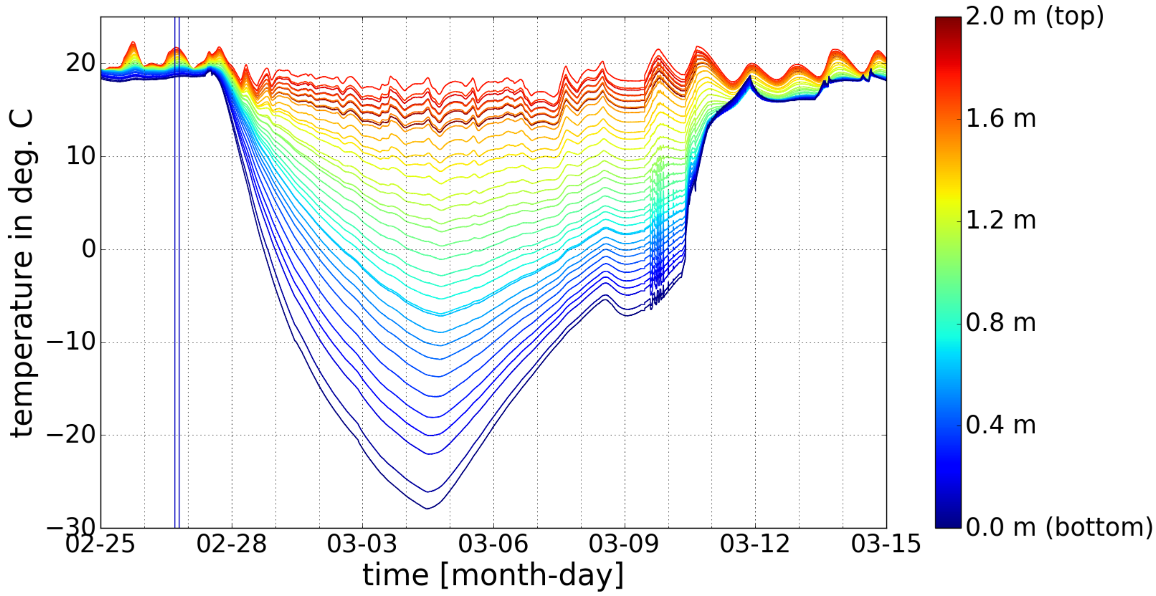

Figure 4.8: Evolution of the temperature along the ribbon chain of 36 temperature sensors in the purity monitoring chimney during the first cool down and subsequent warm up of the detector.

Chapter 5

Read-out of charge signals and induced crosstalk

It is commonly assumed that a SNR of 10 on all channels of the anode is required to provide accurate hit finding in the reconstruction software to precisely reproduce the 3D event tracks. The employed anodes in the $3 \times 1 \times 1$ m^3 detector were carefully designed to provide a capacitance to ground of only 150 pF/m in order to keep the capacitive crosstalk to a minimum. This type of anode, although characterized well on a smaller scale of 10×10 cm^2 in a 3 liter dual phase TPC [12], has never been employed and operated on such a large scale as on the 3×1 m^2 CRP of the detector. In this chapter the response of the anode in terms of noise and crosstalk is described and analyzed. To push our understanding further, capacitance and pulsing measurements were performed on a single anode module which were compared to a simplified equivalent circuit model, described in Sections 5.4 and 5.5.

5.1 Noise measurements and reduction through Fourier filter

Prior to the cool down of the detector, noise measurements were performed on the anode to study the noise on all channels in both views. As described in Section 3.5, to achieve a good SNR, there are two parameters, the gain provided by the LEMs and the introduced noise on the strips of the anode, which need to be maximized and minimized respectively. In this section, the noise introduced from several components of the detector is studied and I show that we can filter out some high frequency components by applying a low-pass filter and improve the SNR. To minimize the noise at the level of the anode, there are two conditions that need to be met: adequate shielding of slow control and signal cables needs to be provided to avoid ground loops, and the capacitance of each strip to the rest of the detector needs to

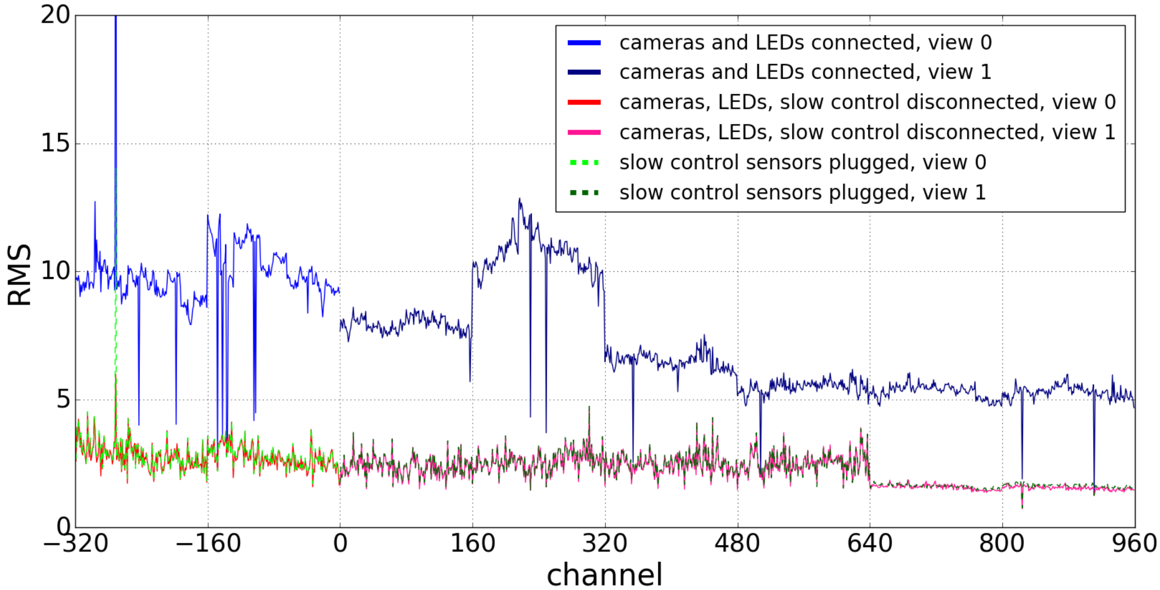

Figure 5.1: Noise measurement with cameras, LEDs and slow control sensors connected (blue), with only slow control sensors connected (green), and slow control sensors, cameras and LEDs disconnected (red). Shown is the RMS of all channels with channels in view 0 running from -320 to 0 and channels in view 1 running from 0 to 960.

be minimized to avoid inducing unwanted signals on other channels and keep the attenuation of the signals low.

5.1.1 Noise measurements

Several runs were taken at varying conditions with different components, such as the temperature and pressure sensors, the PMTs or the high voltage, being switched on or off in order to determine their impact on the noise. Each run consists of several hundred events, with each event spanning a time interval of 0.667 ms and having 1667 time bins with a duration of 400 ns each. Thus the sampling rate is 2.5 MHz. A significant amount of effort has been put into grounding different metal components of the detector to reduce their contribution to the noise and shielding slow control and signal cables from each other. Several runs were also taken with conditions as close as possible to the final configuration during operation. Figure 5.1 shows the root mean square value of all channels in view 0 and 1 for one event of runs with the slow control cables plugged and unplugged, and the cameras and LEDs in the tank vessel connected. The RMS of one channel is defined as:

$$RMS = \sqrt{\frac{1}{N}\sum_{i=1}^{N}(x_i-\mu)^2} \tag{5.1}$$

where N is the number of time bins (1667 in our case), $\mu = \frac{1}{N}\sum_{i=1}^{N} x_i$ is the mean value and x_i are the measured ADC counts. The average RMS values of all channels are given in Table 5.1 for the three considered runs.

Conditions	RMS view 0	RMS view 1	combined RMS	Ratio between RMS of both views
cameras, LEDs and slow control connected	9.78	6.84	7.57	1.43
cameras and LEDs disconnected, slow control connected	2.85	2.22	2.38	1.28
cameras, LEDs and slow control disconnected	2.78	2.17	2.33	1.28

Table 5.1: RMS values of view 0 and 1 for varying conditions. All numbers given in ADC counts.

5.1.2 Fourier transform and noise reduction

Some components were found to introduce a high level of noise leading to an RMS value of over 10 ADC counts, which was also present during the pulsing of the anode in the detector, performed to obtain an accurate calibration and measure its response to a given input of charge, as described in Section 5.2. In order to reduce this noise and increase the SNR, the Fourier transform was taken of signals on each channel and a low-pass filter was applied. Taking the Fourier transform can also help in identifying the source of the noise, by identifying all frequencies that contribute to the signal.

Applying a low-pass filter encompasses taking the fast Fourier transform, a very fast algorithm for computing the discrete Fourier transform, of the signals, making cuts above a certain frequency, i.e. setting all frequency components to zero for frequencies higher than a specified threshold, and taking the inverse FFT. Thus the original signal without its high frequency components is recovered, leading to a smoothing of the signal by removing the short term fluctuations and leaving the longer term trends.

For a sequence of N complex numbers $x_0,\ x_1, \cdots, x_{N-1}$, the discrete FFT returns another sequence of N complex numbers $X_0,\ X_1, \cdots, X_{N-1}$, defined by:

$$X_k = \sum_{n=0}^{N-1} x_n \cdot e^{-2\pi ikn/N} \tag{5.2}$$

When the FFT is computed for a purely real input, as is the case for the signal data, the output is Hermitian-symmetric, i.e. the negative-frequency terms are just the complex conjugates of the corresponding positive-frequency terms, and are therefore redundant. Thus only the positive frequency terms of the FFT are of interest and after its application, a sequence of 834 complex numbers is obtained from the 1667 time bins per event. As the sampling rate is 2.5 MHz, these 834 frequency components correspond to frequencies between 0 and 1.25 MHz, with 1.25 MHz being the highest resolvable frequency. A map of all channels and their corresponding frequency contributions is given in Figure 5.2 for the previously discussed runs, one with cameras and LEDs connected (top) and one with cameras, LEDs and slow control sensors disconnected (bottom). The map shows that certain frequency components

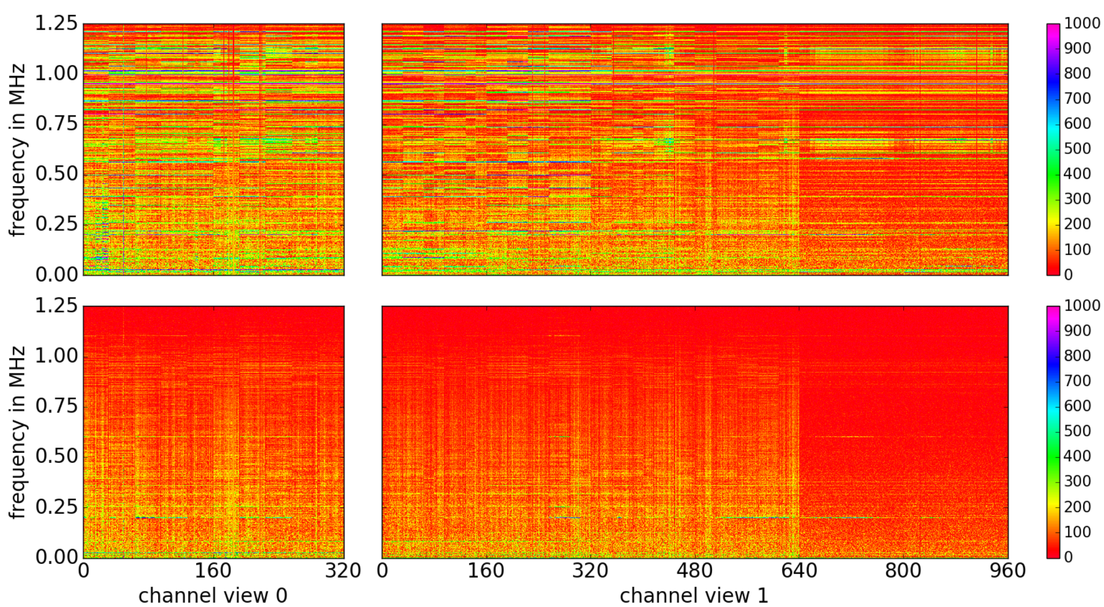

Figure 5.2: Frequency map of runs with cameras, LEDs and slow control sensors connected (top) and disconnected (bottom). The contribution of each frequency component is indicated by the color scale, with channel numbers on the x-axis (for view 0 and 1) and frequency on the y-axis.

are much more present with the LEDs, cameras and slow control sensors connected, especially for frequencies above 0.6 MHz which seem to have had a particularly large impact on the noise in both views. Thus the application of a low-pass filter with a cut-off threshold below those frequencies would provide a significant noise reduction with lower RMS values, as described below. Table 5.2 shows the reduction of the RMS values of both runs considered after the application of the low-pass filter with various frequency cut-off thresholds. Figure 5.3 shows

	no cuts	1.0	0.9	0.8	0.7	0.6	0.5	0.4	0.3	0.2	0.1
connected	7.57	6.93	3.95	3.50	3.29	3.03	2.78	2.60	2.36	1.96	1.47
disconnected	2.33	2.30	2.24	2.20	2.16	2.09	2.01	1.89	1.71	1.45	1.12

Table 5.2: Average RMS values of all channels for one event from runs with cameras, LEDs and slow control sensors connected (top) and disconnected (bottom), given in ADC counts, after application of a low-pass filter for various frequency cutoffs, given in MHz.

the noise introduced on channel 100 in view 0 for one event in runs with cameras, LEDs and slow control sensors connected and disconnected as well as the signal after the low-pass filter has been applied for several cutoff frequencies. With lower thresholds for the low-pass filter,

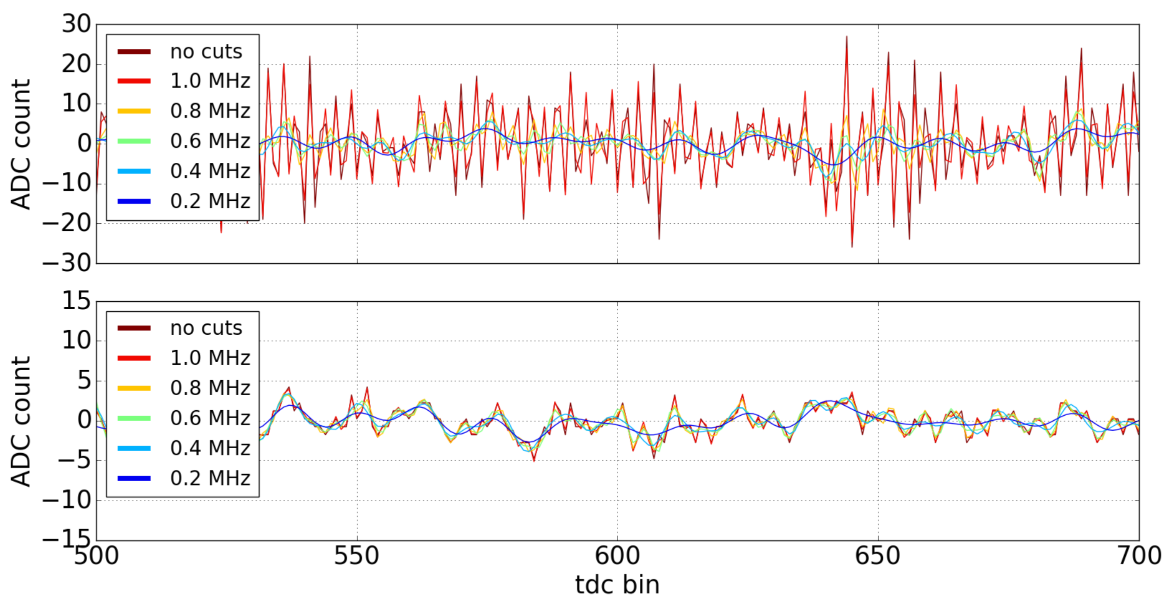

Figure 5.3: Typical signals on channel 100 in view 0 for runs with cameras, LEDs and slow control sensors connected (top) and disconnected (bottom) before and after the application of a low-pass filter with various frequency cut-offs.

the signal gets smoothed out more and the RMS is reduced. The effect of these filters applied to signals with a pulsed charge input is described in Section 5.2.

5.2 Response of the 3×1 m^2 charge readout plane to a calibration pulse

Before the cool down of the detector was initiated, all channels on the anode were pulsed in multiple runs, using a pulse generator, in order to measure the response of the electronics on each channel to a known amount of charge injected and to identify dead channels. Of particular interest is the crosstalk between different anode strips, which describes any induced signals from a pulsed strip onto other strips. Crosstalk can occur at the level of the anode, through capacitive couplings between individual strips or at the readout stage through complex couplings between the preamplifiers, located in the SGFT chimneys. A detailed analysis of the observed crosstalk is given in Section 5.3.

In each run, different sets of channels were pulsed, as described further down. A 1 pF capacitor was placed in between the pulse generator and the connection to the anode channels in order to inject a specific amount of charge and thus produce a signal similar to the ones expected from the drift electrons of an ionizing particle when the detector is in operation. The pulse generator produces a square wave with a low frequency of about 3 Hz, amplitude of 150 mV and rise/fall times of 100 ns and a 50 % duty cycle. This corresponds to a charge of 150 fC injected through the capacitor, on the rising and falling edges of the square wave pulse. The response of all strips was recorded during the time of voltage change. Each run consists of a few hundred events, with each event recording the response of all channels over a time period of 0.67 ms, with 1667 time bins of 400 ns. The trigger for each event was set up such that the pulse always occurred at a time bin around 760. Figure 5.4 shows the shape of the pulse with the chosen eventwindow. Due to the setup of the connection between the pulser and the channels, it is only possible to pulse a minimum of 32 neighboring channels. The pulser is connected to a connector of 32 strips, indicated in gray, opposite the colored connectors leading to the preamps, in Figure 3.9. A simplified equivalent circuit of the pulsing scheme and the anode strips is given in Figure 5.5. Here the charge is injected through the 1 pF capacitor C_{inj}, located after the pulser. A single strip is shown in blue, with a high impedance draining resistor R_{drain} of 500 MΩ. The draining resistor provides a means of removing the excess charge, which builds up on the strips after the arrival of drift electrons, over a time period much longer than the length of a signal induced by ionizing radiation. A decoupling capacitor is located at the end of each channel with a capacitance of 2.2 nF. This capacitor is part of the readout electronics design and decouples any potential DC voltages from the induced signals on the strips in case of a potential difference between the anode with

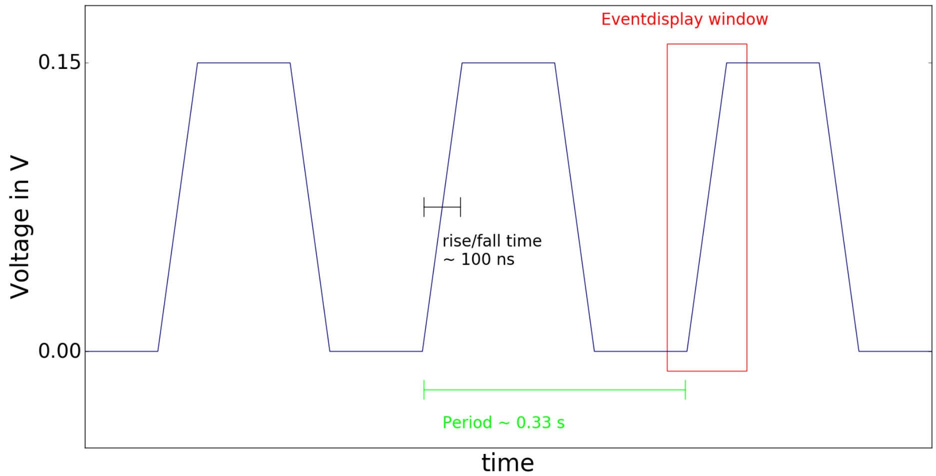

Figure 5.4: Shape of the waveform generated by the pulse generator (not to scale), with rise/fall times of 100 ns, a frequency of 3 Hz and an amplitude of 150 mV. The eventwindow is chosen to coincide with the rising edge of the pulse.

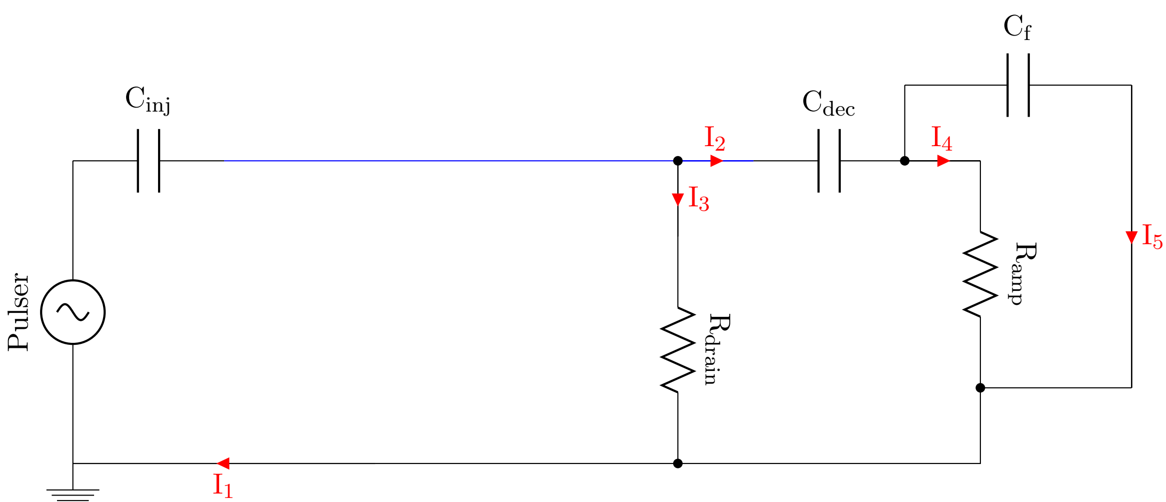

Figure 5.5: Simplified equivalent circuit of the pulsing scheme. Charge is injected onto one anode strip (blue) through the pulser and the 1 pF capacitor. The preamp is modeled as a low impedance resistor to ground with a feedback capacitor across.

respect to ground. The preamp is modeled by a low impedance resistor to ground of order 10 Ω and a feedback capacitor with a capacitance of 1 pF to achieve a high amplification of the signal.

variable	value in μs
τ_1	2.84 ± 0.09
τ_2	0.47 ± 0.02
τ_3	0.46 ± 0.02

Table 5.3: Average values over 32 channels of the shaping time constants appearing in the preamplifier response, as reported in [26].

5.2.1 Response of electronics to injected signal

As one time bin of the DAQ is 400 ns and the rise time of the injected 150 mV pulse is 100 ns, it can be considered as the equivalent of a delta peak with regard to the charge injection. The preamplifier output is continuously digitized by 12-bit ADCs with a range of 0-2.2 V, allowing for a total of 4096 ADC counts, located on the top cap in accessible crates near the SGFT chimneys. The preamplifier response to a delta-like charge pulse at $t = 0$ can be approximated by [26]:

$$h(t) = \frac{\tau_1(\tau_2-\tau_3)e^{-t/\tau_1}+\tau_2(\tau_3-\tau_1)e^{-t/\tau_2}+\tau_3(\tau_1-\tau_2)e^{-t/\tau_3}}{\tau_1^2(\tau_2-\tau_3)+\tau_2^2(\tau_3-\tau_1)+\tau_3^2(\tau_1-\tau_2)} \quad \text{for } t \geq 0 \tag{5.3}$$

$$h(t) = 0 \quad \text{for } t < 0 \tag{5.4}$$

which gives 1 if integrated with respect to t. The values of the time constants τ_i depend on the characteristic capacitances and resistances in the preamplifiers. An estimation of their values comes from a fit of $h(t)$ to the preamplifier output after a very short pulse and are given in Table 5.3.

Figure 5.6 shows the response of the electronics to the injected pulse as well as the theoretical response, according to Equations 5.4 and 5.4, for both view 0 and view 1 pulsed. Shown is a single pulsed channel, characteristic of all the 32 pulsed ones for a run with channels 288-319 in view 0 pulsed and a run with channels 0-31 in view 1 pulsed. The sensitivity of the electronics is 0.15 fC per ADC count for a delta-like pulse. With the pulse height of the signals shown being 434 and 771 ADC counts, this corresponds to a measured charge of 65.1 and 115.7 fC for views 0 and 1 respectively, which is to be compared to the injected 150 fC. As the response of the electronics should be identical for all strips, attenuation must occur due to crosstalk at the level of the anode due to its intrinsic design. The attenuation in terms of charge loss over the 3 meter long strips is 2.48 times as much as for the 1 meter strips, confirming the charge loss through capacitive couplings to other strips and an attenuation that scales with the length of the anode strips.

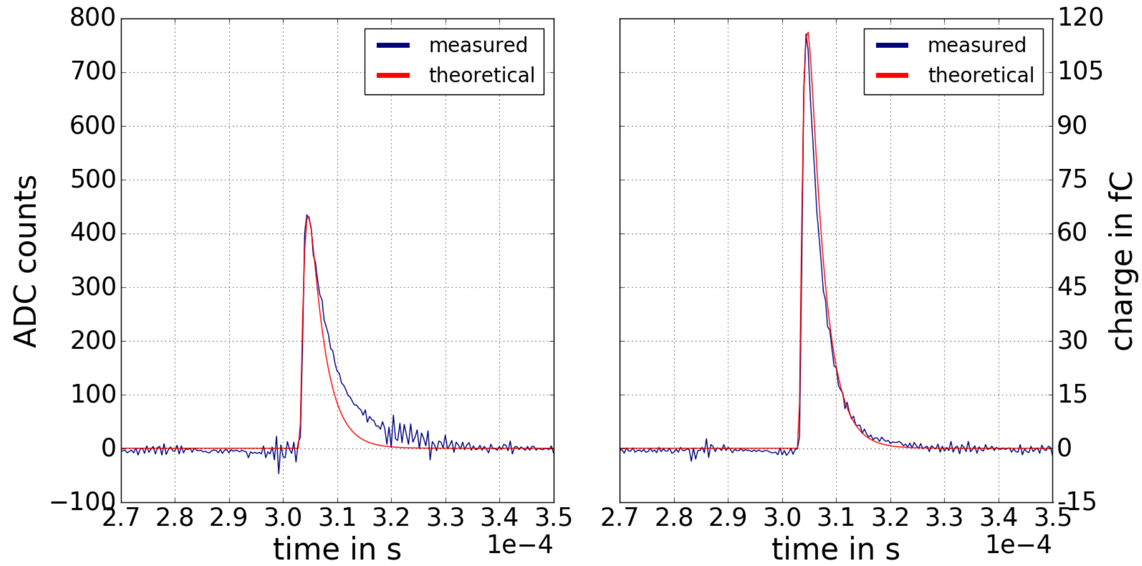

Figure 5.6: Response of the preamp and ADC to the injected 150 fC pulse (blue) as well as the theoretical response, according to Equations 5.4 and 5.4 for pulsed channels in view 0 (left) and view 1 (right).

5.2.2 Effect of software low-pass filter on signal

During the pulsing, a large amount of noise was observed on all strips with an RMS value of 9.0 ADC counts for the pulsed channel 288 in view 0, shown in Figure 5.6, for the time before and after the pulse. The low-pass filter, described in Section 5.1.2 was hence applied in order to increase the SNR and study its effect on the shape of the waveform. Figure 5.7 shows the obtained signal on channel 288 in view 0, which was pulsed together with channels 289-319 in this run as well as the signal after the application of the low-pass filter for various frequency cut-offs. The maximum height of the peak and its integral for tdc bins between 730 and 850, as well as the RMS of the noise before and after the pulse, are given in Table 5.4 for various cut-off frequencies of the low-pass filter. Thus the height of the peak and its integral are affected by only 0.5 % and 0.03 % respectively for frequency cuts above 0.3 MHz, with the maximum resolvable frequency in one event being 1.25 MHz. Figure 5.7 also shows, that the signal waveform stays relatively unaffected for this frequency threshold, while the RMS of the noise decreases by a factor of 2.6, leading to more than double the SNR. This shows that the application of a low-pass filter can drastically improve the signal quality, thus leading to better 3D reconstruction of events, using relatively little computational resources.

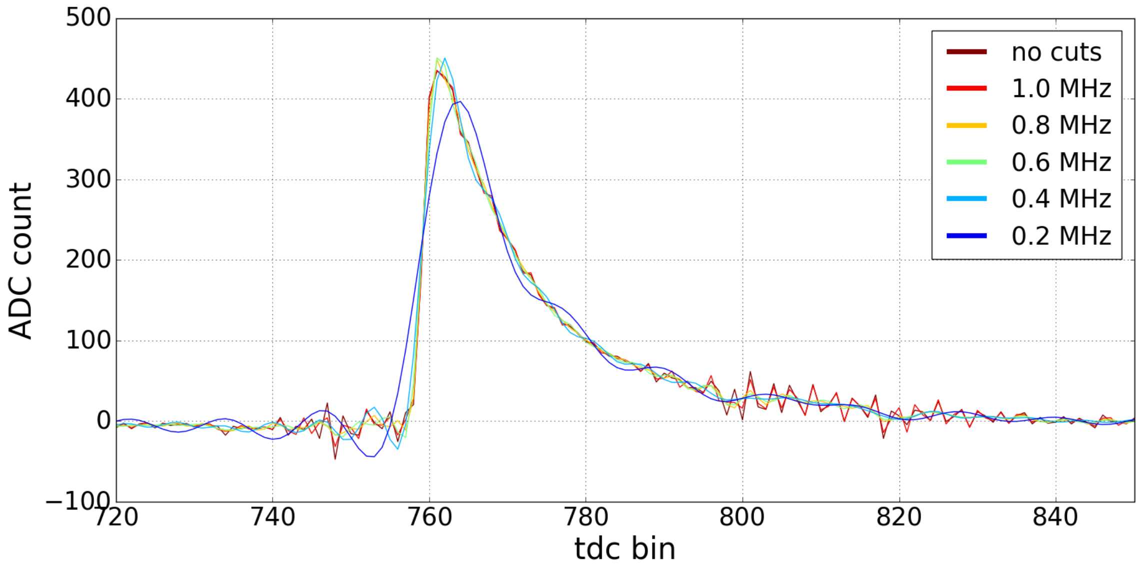

Figure 5.7: Signal of pulsed channel 288 in view 0 for a run with channels 288-319 pulsed as well as signal after application of a low-pass filter for different cut-off frequencies. The channels were pulsed at a tdc bin of about 760 (1 tdc bin has a duration of 400 ns).

cutoff frequency	no cuts	1.0	0.9	0.8	0.7	0.6	0.5	0.4	0.3	0.2	0.1
peak maximum	434	435	447	449	453	451	450	451	432	397	307
integral of peak	6796	6797	6797	6798	6798	6800	6799	6795	6798	6808	6877
RMS of noise	9.0	7.6	5.1	4.4	4.2	4.0	3.8	3.6	3.4	3.1	3.1

Table 5.4: Properties of the waveform of pulsed channel 288 after application of low-pass filter for various frequency cut-offs. All numbers are in ADC counts, except the cut-off frequencies, which are given in MHz.

5.3 Analysis of crosstalk

Crosstalk describes any induced signals on channels of the anode arising from currents on other strips, due to pulsing of specific amounts of charge, as described in Section 5.2, or drift electrons arriving on the CRP during operation. During the pulsing measurements, described in Section 5.2, some level of crosstalk was observed on all non-pulsed strips simultaneously with the arrival of the signal on the pulsed strips. It is important to quantify this crosstalk in order to get the correct attenuation of the signal, due to charge loss onto other strips, to achieve good energy resolution and to build better software models, which ignore these signals on other channels to obtain good 3D reconstruction of events.

The observed crosstalk seems to be induced through two different modes. As mentioned in Section 5.2.1, attenuation of the signal must occur at the level of the anode due to its intrinsic design through capacitive couplings between the pulsed strip and other non-pulsed strips. Figure 5.8 shows a schematic of the strip layout on the anode. Each strip has a certain ca-

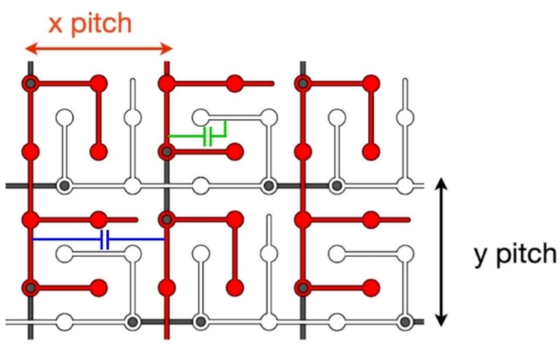

(a) Schematic of strip layout on the anode. Capacitances between parallel strips are indicated in blue, for perpendicular strips in green.

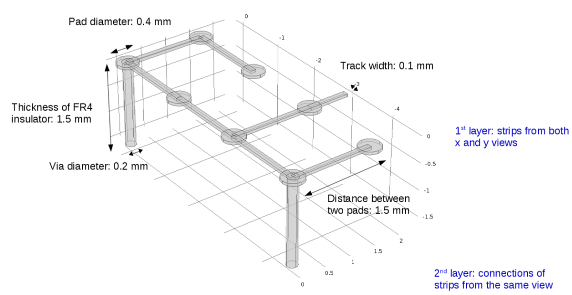

(b) 3D geometry of an anode pixel, taken from [27].

Figure 5.8: Schematic layout of the anode and 3D geometry. Each pixel consists of two short strips, one for each view, colored in red and white in the left Figure. These are connected together through wires passing underneath the strip layer.

pacitance to other parallel strips in its vicinity and to all the perpendicular strips it crosses and thus signals are induced on other strips through capacitive couplings. The second mode through which crosstalk is induced is at the level of the preamps in the SGFT chimneys. Each of the five cards in each chimney holds the preamps for 64 channels, grouped in two connectors of 32 channels each, as shown in Figure 3.9. Each connector connects to strips from a different $0.5 \times 0.5\ \mathrm{m}^2$ anode module. A signal with a different waveform is observed on the channels of the counter connector to the pulsed connector, compared to the induced signals seen on all other strips. Figure 5.9 shows a channel map of all channels averaged over 218 events of one run, where channels 0-31 in view 1 were pulsed. Crosstalk can be observed

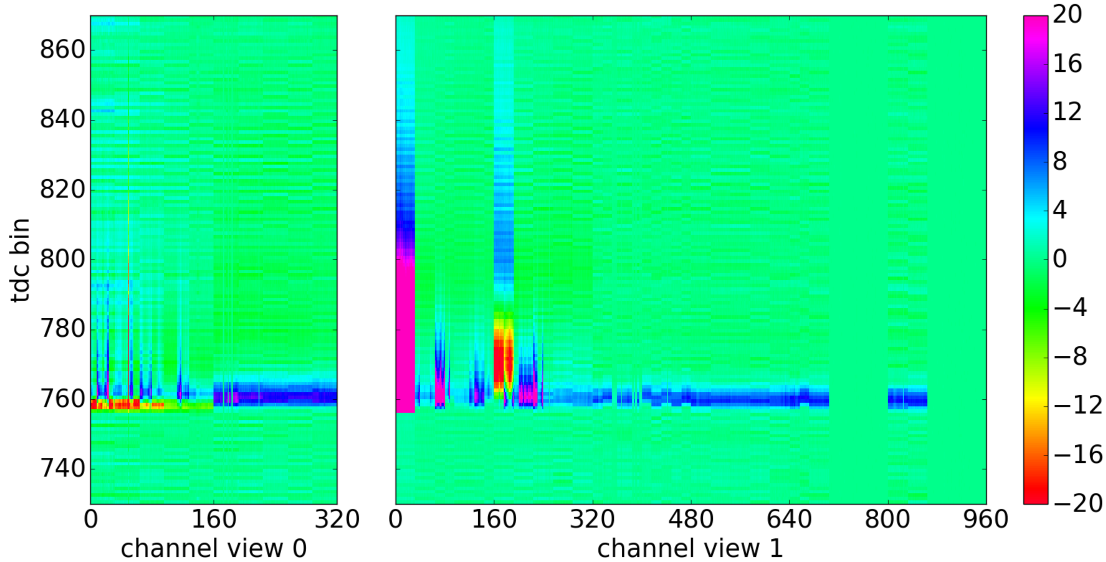

Figure 5.9: Channel map of all channels in view 0 (left) and view 1 (right), averaged over the 218 events of a run with channels 0-31 in view 0 pulsed, highlighting the induced crosstalk.

on all other perpendicular channels with regard to the pulsed one and on the parallel channels in the same view where the distance from the pulsed strip does not seem to affect the induced signal height much. In addition a large signal is observed on channels 160-191, which lead to the counter connector on the same card as the pulsed channels. Some channels in view 1 do not show any response, as the connectors were not plugged in during the pulsing.

Figure 5.10 shows the induced signals on a few other channels in both views for the previously described run with channels 0-31 in view 1 pulsed, with the signal averaged over 218 events. The induced crosstalk for all runs with 32 channels simultaneously pulsed is at the level of a few percent in terms of the height of the waveform of the induced signals compared to the pulsed channels for both view 0 and view 1. The induced waveforms on channels leading to the counter connector of the pulsed one are quite distinct from all others, meaning that crosstalk has to occur at the level of the preamps. The overall height of the induced signals varies from strip to strip, however, is fairly similar for strips parallel and perpendicular to the pulsed ones, as can be seen in Figure 5.10. In order to quantify and understand the cause of the crosstalk at the level of the anode, capacitance measurements were performed on one anode module as well as pulsing measurements, where a single channel was pulsed through a capacitor and the induced signals on other strips were measured. These pulsing measurements are described in the next section and are to be compared with the simultaneous pulsing of 32

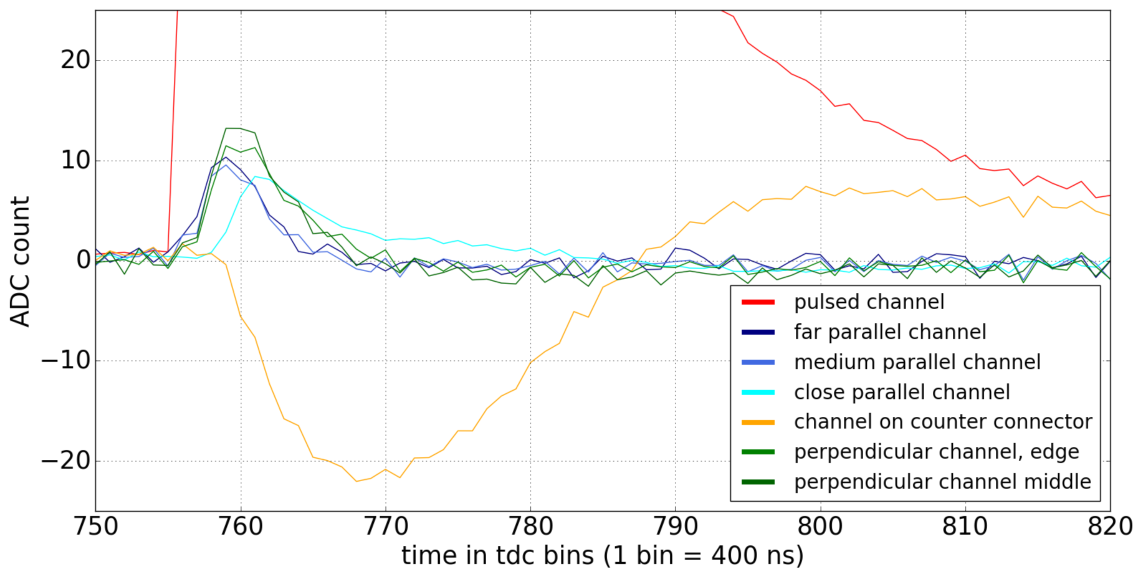

Figure 5.10: Induced crosstalk on other channels for a run with channels 0-31 in view 1 pulsed with an injected charge of 150 fC. The waveforms have been averaged over 218 events.

strips on the anode in the detector.

5.4 Capacitance measurements on a 50×50 cm^2 anode module

The aforementioned capacitive crosstalk is believed to be caused by capacitive couplings between the strips on the anode. To study this behavior, the capacitance between strips has been measured on one 50×50 cm^2 anode module, using a Sourcetronic ST2831 LCR meter, in a clean room, located next to the detector in order to include the capacitances in a simplified equivalent circuit model and compare it to pulsing measurements done on a single anode module, as described in Section 5.5. For the setup, the anode module was placed on an isolated cardboard box, in order to reduce any capacitances arising from metal components in its immediate vicinity. The LCR meter has been tested on a capacitor and resistor with known capacitance and resistance respectively. Figure 5.11 shows the setup as well as the LCR meter with the calibration capacitor. The anode module consists of a PCB with 160 strips in each view. These are made up of individual pixels in the bottom layer of the anode (facing the LEM) that the electrons are collected on. Each pixel is made up of two short strips for the two views with three fingers each. The short strips in each view are connected together through wires 1.5 mm above the layer of the short strips. A schematic of the strip layout on the anode module is shown in Figure 5.8.

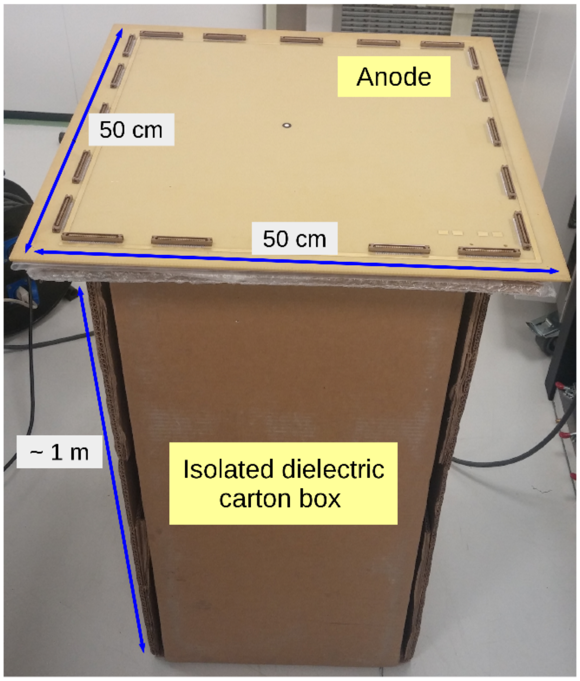

(a) Experimental setup with the anode module placed on an isolating cardboard box.

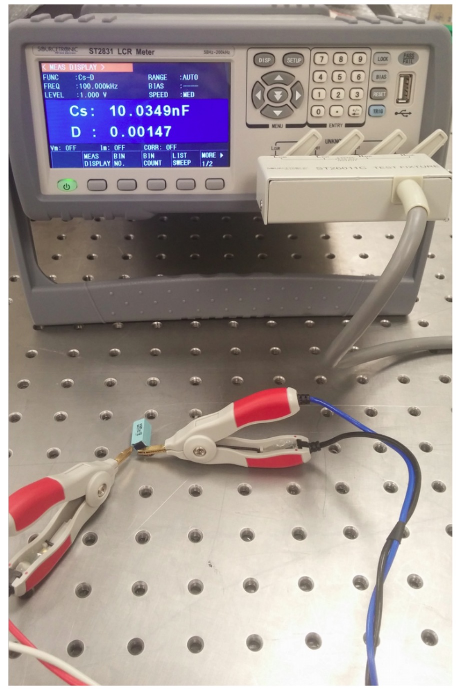

(b) Sourcetronic ST2831 LCR meter with calibration capacitor.

Figure 5.11: Experimental setup of the capacitance measurements on one anode module.

Each strip has various capacitances to different components. These consist of the capacitance to other strips, which differs, depending on whether it is parallel or perpendicular to the considered strip and their respective distance from each other in the case of parallel strips, and the capacitance to a metal back strip of each anode module, which runs along the edges of each module. As all strips in the detector lead to the preamps in the SGFT chimneys, which provide a virtual ground, the total capacitance to ground of a single strip, called C_{det}, consists of the capacitances to all other strips and the capacitance to the anode back strip.

To measure the capacitance between two parallel or perpendicular strips, all other strips as well as the anode metal back strip were connected to ground (the common ground of the LCR meter) and the probes were placed on the two strips considered. This setup is shown in the schematic of Figure 5.12a. The capacitance between parallel strips was found to decrease rapidly with increasing distance between the strips; the capacitance between two neighboring strips was measured to be 7.6 pF but is less than 1 pF for third closest strips and falls below 0.1 pF for strips further than 30 strips from the measured one. This can be seen in Figure

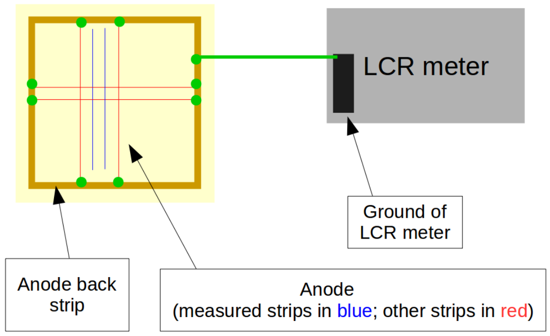

(a) Setup for measuring the capacitance between two parallel strips (similar setup for perpendicular ones).

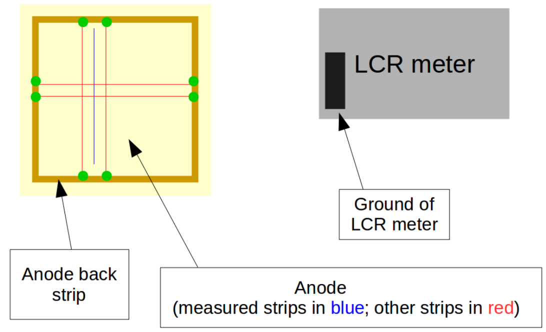

(b) Setup for measuring the capacitance of one strip to all other strips and the anode metal back strip.

Figure 5.12: Schematic of the experimental setup for capacitance measurements with grounding of various components.

5.13 which shows the measured values between two closest strips up to 31st closest strips for different frequency settings of the LCR meter. Overall the capacitive coupling between

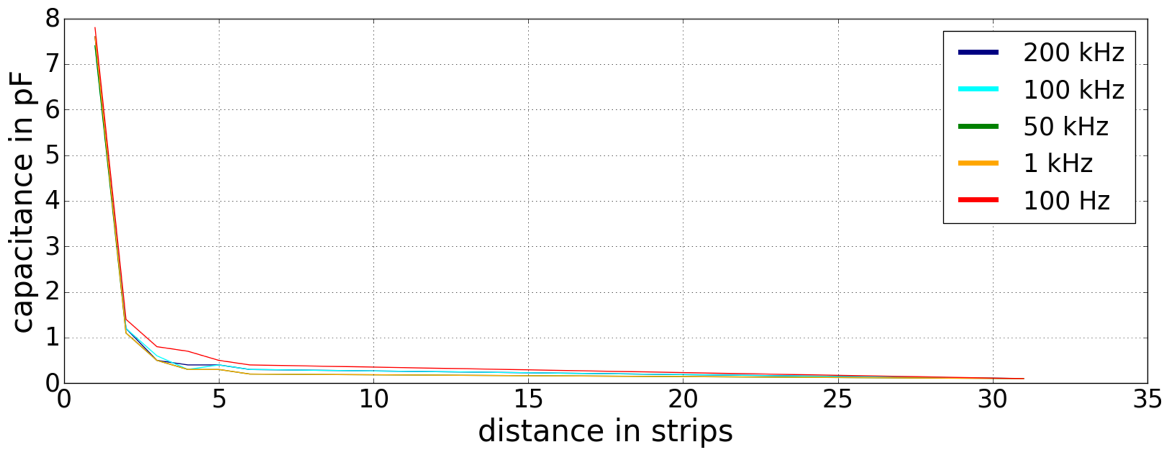

Figure 5.13: Measured capacitances between parallel strips for varying distances and different frequency settings for the LCR meter.

parallel strips only seems to be relevant for strips that are separated by no more than 10 strips.

In contrast to the capacitances between parallel strips, the capacitances between two perpendicular strips were found to be constant and do not depend on their respective location on the anode. The capacitance between two perpendicular strips on the edges of the anode, one strip on the edge and one in the middle, and two strips in the middle, in their respective views, was found to be constant, at 0.4-0.5 pF. The setup used for the perpendicular capacitance measurements is the same as the one for parallel ones, shown in Figure 5.12a, with all other strips grounded to the metal back strip and to the ground of the LCR meter.

To measure the capacitance of one strip to all other strips, all strips except one were connected together and to the metal back strip, but not to the ground of the LCR meter, in order to not cause a short circuit. The probes were placed on the one isolated strip and on the metal back strip to measure the capacitance, as shown in the schematic of the setup in Figure 5.12b. This capacitance of one strip to all other strips was found to be 78 pF for one anode module or 156 pF/m. A summary of all measured capacitances of one strip to various components is given in Table 5.5. From the table we can see that the total capacitance of one strip to the

	C_{det}	C_{ground}	$C_{\perp}$	$C_{\parallel 1}$	$C_{\parallel 2}$	$C_{\parallel 3}$	$C_{\parallel 4}$	$C_{\parallel >4}$
measured capacitance in pF	78	1.7	0.4-0.5	7.6	1.2	0.5	0.4	< 0.3
capacitance from COMSOL simulations in pF	36.14		0.15	1.3				

Table 5.5: Measured capacitances between one anode strip and various components on a single anode module as well as simulated ones [27] for C_{det}, $C_{\perp}$ and $C_{\parallel 1}$. C_{det} is the capacitance to all other grounded strips, C_{ground} is the capacitance to the metal anode back strip, $C_{\perp}$ is the capacitance between perpendicular strips and $C_{\parallel i}$ is the capacitance between the ith closest parallel strips.

rest of the detector, called C_{det} really is the sum of the capacitances of the strip to all other components, as 160×0.4 pF + 1.7 pF + $2 \times$ (7.6 pF + 1.2 pF + 0.5 pF + 0.4 pF + $\cdots$) ≈ 78 pF.

Extensive numerical simulations have been performed, using the COMSOL Multiphysics software, to verify the measured values of the capacitances [27]. The extrapolated values are given in Table 5.5. Even though the values do not correspond directly to the measured ones, the ratios between the various capacitances agree with the measurements with the capacitance between parallel strips being of order ten times that between perpendicular strips and the capacitance to ground C_{det} being the dominant one.

5.5 Pulsing of a single anode strip on the 50×50 cm^2 anode module

In order to understand and analyze the capacitive crosstalk observed during the detector pulsing, described in Section 5.2, pulsing measurements were performed on a single 50×50 cm^2 anode module in the clean room, located next to the detector. Measurements taken on this smaller setup allowed for more flexibility in the adjustments of parameters such as the injected charge, the grounding of various components and being able to pulse a single strip. The drawback is that this setup can only give the response of a single anode module which has to be extrapolated onto the twelve modules employed in the detector. In addition, the induced currents are measured using a commercial oscilloscope and the charge sensitive preamplifiers in the detector can not be taken advantage of.

5.5.1 Experimental setup

In order to replicated the setup in the detector as much as possible, all strips on the anode module were connected through a resistor to a common ground on one end, to simulate the impedance of the preamps in the SGFT chimneys, which provide a virtual ground. The anode was placed on an isolating cardboard box, away from any metal components (shown in Figure 5.11a), like in the setup for the capacitance measurements, described in Section 5.4. The induced currents on all strips could therefore be measured directly using an oscilloscope and placing the probes across the resistor. The oscilloscope measures the voltage drop through the resistor and the current is thus given by Ohm's law: $I = V/R$. With this setup it was possible to pulse a single strip through a 1 nF capacitor, as opposed to the simultaneous pulsing of 32 channels in the detector, using a pulser with a square wave output with adjustable frequency, rise/fall times and peak-to-peak amplitude. The pulsed strip was terminated at the other end with a 150 Ω resistor, connected to ground. Connecting all other 159 + 160 strips of the two views through a resistor to ground presented a challenge, as each strip would have had to be connected individually to a single resistor, which all lead to a common ground. With a readout pitch of 3.125 mm/strip, spatial as well as time constraints only allowed for a total of 128 individual strips to be connected in this way. All other strips were connected together into groups of 16 strips which were then connected to a single resistor. The connections of all strips to ground through the resistor were verified using a multimeter. Figure 5.14a shows a schematic of the experimental setup with 64 strips in each view connected individually to 150 Ω resistors (black), one of them being the pulsed strip, placed in the center of those 64 strips (red), and all other strips (blue), being connected in groups of 16 to the common ground through 150 Ω resistors. To measure the voltage drop across the resistors and thus

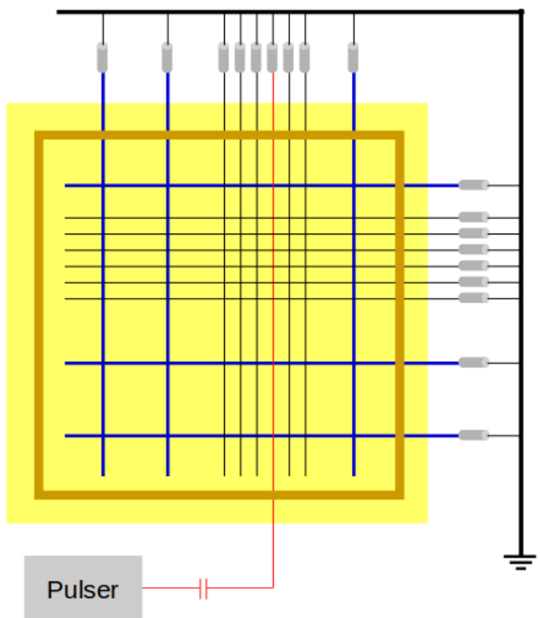

(a) 64 strips in both views are terminated individually by a resistor to ground (black). All other strips are connected into groups of 16 (blue) which are terminated through a resistor to ground.

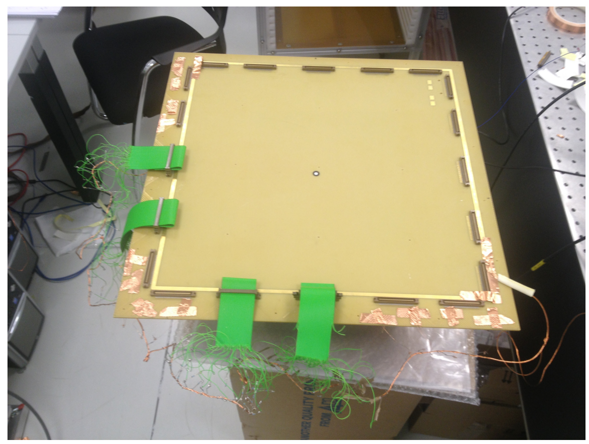

(b) Picture of the pulsing setup used with four connectors terminating 64 individual strips in both views through a 150 Ω resistor to ground.

Figure 5.14: Experimental setup used to measure the response of the strips for pulsing one strip on a single anode module. The charge is injected onto one strip (red in left Figure) through a capacitor connected to the pulser.

obtain the induced crosstalk, a Lecroy WR104MXI digital oscilloscope was used with 1 MΩ high impedance probes, which were placed across the resistors, shown in gray in Figure 5.14a. A square wave was used for the pulser output with a low frequency of the order of 100 Hz and rise/fall times of 100 ns, as in the pulsing of the detector. The general shape of the square wave output of the pulser is similar to the one shown in Figure 5.4, only with different parameters. The eventdisplay window in that figure corresponds to the time window chosen on the oscilloscope. The peak-to-peak amplitude could be set for values between 0 and 10 V. The oscilloscope was set up to trigger on the rising edge of the square wave and a time window of a few hundred nanoseconds was chosen. The obtained signals are shown and described in Section 5.5.2.

5.5.2 Response of the anode module to pulsing of one strip

In this Section, the responses of the pulsed strip and non-pulsed strips in both views are described and analyzed. The obtained signals are compared to the currents obtained from solving the differential equations from a simplified equivalent circuit model which uses the previously measured capacitances between individual strips, described in Section 5.4.

A simplified equivalent circuit for the setup of the pulsing measurements of one anode module, as described in Section 5.5.1, is given in Figure 5.15. Shown is one strip of the anode which

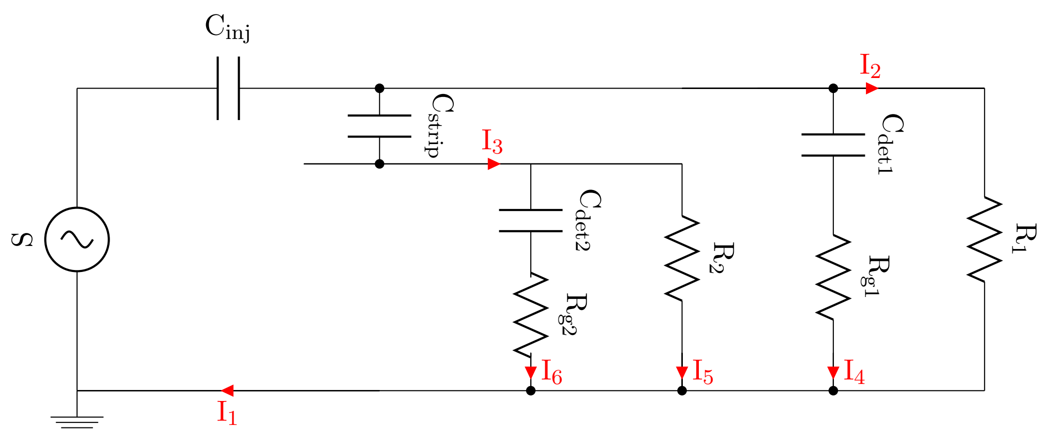

Figure 5.15: Equivalent circuit model for two anode strips during pulsing measurements on one anode module. Through the capacitor C_{inj}, a specific amount of charge is injected onto one strip, which has a capacitive coupling to another strip. Both strips are terminated by a resistor to ground and have a capacitance to the all other components, called C_{det}.

is pulsed by the source S, the pulser, through the 1 nF capacitor C_{inj}. The pulsed strip is terminated by a 150 Ω resistor to ground. It has a capacitive coupling to another strip C_{strip}, which is terminated by another 150 Ω resistor to ground. The value of C_{strip} depends on which strip is considered with regard to the pulsed strip and is given by the measured values of the capacitance between strips, given in Table 5.5. Both considered strips have capacitive couplings to all other strips of the anode, where C_{det} was found to be 78 pF, as described in Section 5.4. All of these components are terminated through 150 Ω resistors to ground. The set of linear ordinary inhomogeneous differential equations obtained from this circuit according to Kirchhoff's laws are:

$$I_1 = I_2 + I_3 + I_4 \tag{5.5}$$

$$I_3 = I_5 + I_6 \tag{5.6}$$

$$\frac{d}{dt}V_S - \frac{1}{C_{inj}}I_1 - \frac{1}{C_{strip}}I_3 - \frac{1}{C_{det2}}I_6 - R_{g2}\frac{d}{dt}I_6 = 0 \tag{5.7}$$

$$-\frac{1}{C_{det1}}I_4 - R_{g1}\frac{d}{dt}I_4 + R_2\frac{d}{dt}I_5 + \frac{1}{C_{strip}}I_3 = 0 \tag{5.8}$$

$$-R_2\frac{d}{dt}I_5 + R_{g2}\frac{d}{dt}I_6 + \frac{1}{C_{det2}}I_6 = 0 \tag{5.9}$$

$$-R_1\frac{d}{dt}I_2 + R_{g1}\frac{d}{dt}I_4 + \frac{1}{C_{det1}}I_4 = 0 \tag{5.10}$$

where V_S is output voltage provided by the source, the pulser. A numerical solution to this set of differential equations has been computed using the mathematical computation program *Wolfram Mathematica 11.1*. Figure 5.16 shows the measured currents through the resistor of the pulsed strip and the closest parallel strip to it, as well as the current obtained from the numerical solution of the differential equations 5.5 - 5.10, using C_{strip} = 7.6 pF and $C'_{det} = C_{det} - C_{strip}$ = 70.4 pF, as given in Table 5.5. A more detailed plot of the measured

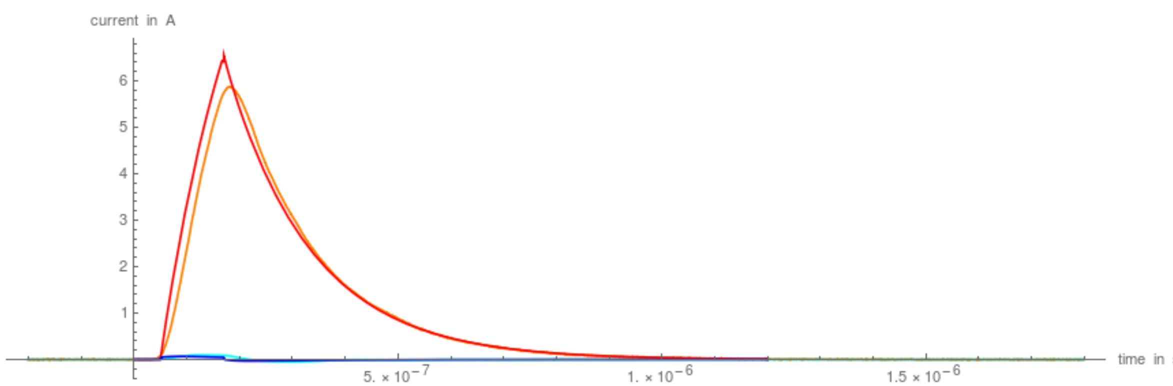

Figure 5.16: Measured current through resistor of pulsed strip (orange) and closest parallel strip (cyan) and theoretical current obtained from numerical solution to system of differential equations (red for pulsed strip, blue for closest parallel one).

and theoretical current induced on the closest parallel strip, as well as the ones for a group of 16 strips perpendicular to the pulsed one, is given in Figure 5.17.

As the level of noise introduced on the probes of the oscilloscope through their proximity to the anode was found to be a few times higher than the voltage measured across a resistor of a single perpendicular strip, an accurate measurement of the induced signals in the perpendicular view could only be obtained by measuring the voltage across a resistor terminating

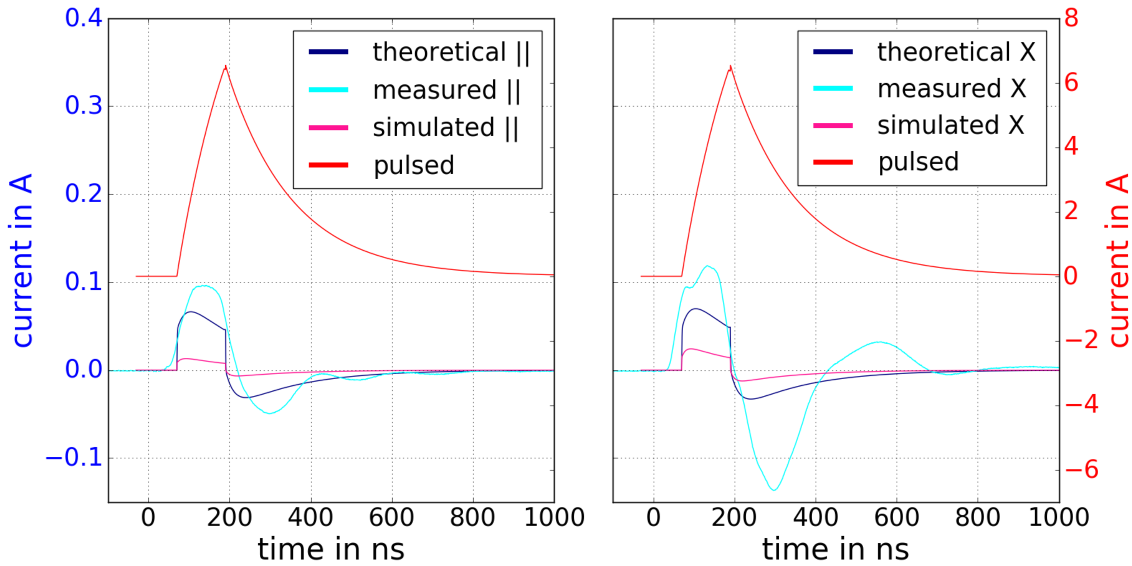

Figure 5.17: Currents through resistors of single closest parallel strip (left) and 16 connected perpendicular strips (right). Shown are the measured currents from the pulsing measurements (cyan), the theoretical currents obtained from numerical solution to system of differential equations with measured capacitances (blue) and the simulated ones (pink) [27]. Also shown, the theoretical current of the pulsed strip (red), with common axis given on the right in red.

16 neighboring perpendicular strips to ground.

The obtained results give us confidence in the accuracy of the capacitance measurements, described in Section 5.4, as well as the equivalent circuit model being able to accurately describe the induced signals on non-pulsed strips of the anode. Extrapolating the results onto the entire anode, composed of 12 anode modules and comparing to the pulsing measurements performed on the anode employed in the detector, described in Section 5.3, confirms that the observed crosstalk on the perpendicular strips, which was of the order of a few percent, is caused by the capacitive couplings between perpendicular strips, with the measured capacitance being 0.4-0.5 pF. The proportion of the signal heights between the induced signals on the group of 16 perpendicular strips and the pulsed strip is 1.82 %, thus it should be 0.114 % for a single perpendicular strip. As 32 neighboring parallel strips were pulsed simultaneously in the detector, the latter proportion is multiplied by 32 to obtain an accurate value of 3.64 %. The induced signals on parallel strips can not be explained directly using this model, as the capacitance between parallel strips was found to decrease rapidly with increasing distance, with values of less than 0.1 pF after the 30th closest strips. The observed level of crosstalk during the pulsing in the detector, however, did not decrease with distance from the pulsed strips, as can be seen in Figure 5.9. This induced crosstalk on further parallel strips, located multiple meters away from the pulsed channels, is thought to be caused by higher order capacitive couplings, where signals induced on non-pulsed channels induce further signals on other channels. As each strip parallel to the pulsed strips couples to all other strips in the other respective view with a capacitance of 0.4-0.5 pF, a total coupling of one strip in view 1 (1 m long strips) to all 320 strips in view 0 (3 m long strips) of 0.114 % $\times$ 320 = 36.4 % is obtained. Using the equivalent circuit model, the proportion of the signal heights on the perpendicular strips is found to be 3.64 %, for the pulsing in the detector with 32 strips pulsed simultaneously. Thus a signal with a height of 36.4 % $\times$ 3.64 % = 1.32 % of the pulsed signal height should be obtained on far parallel strips just through second order coupling. Capacitive couplings at higher orders will further increase the induced signal height on far parallel strips.

Thus the capacitive crosstalk observed at the level of the anode, described in Section 5.3, and found to be at the level of a few percent for all channels in both views, can be explained using the equivalent circuit model and considering second order effects.

Chapter 6

Conclusions

As the $3 \times 1 \times 1$ m^3 detector serves as a test platform for future dual phase LAr TPCs, it is important to learn from its construction, commissioning and operation and implement the successfully tested techniques into the designs of future detectors. In this thesis I studied the pressure and temperature behavior of the tank in warm and during the cool down, the evolution of impurities during the purge of the tank, the expected level of noise during operation and its reduction, and the response of the anode to charge pulsing, which was compared to capacitance and pulsing measurements and an equivalent circuit model. The findings of these investigations are given below.

6.1 Pressures of tank, insulation and SGFT chimneys

It was found, that the pressure in the tank could be kept constant at 1000 mbar over multiple days, with no correlation to the atmospheric pressure and a RMS value of 0.19 mbar, see Section 4.1. A constant pressure is paramount in order to achieve a constant LEM gain, which depends strongly on the gas density, as described in Section 2.3.2.

The insulation of the tank needs to be purged with nitrogen gas in order to avoid liquefaction of oxygen. As leaks were found in the outer structure of the cryostat, a continuous flow of nitrogen needs to be realized, thus keeping the pressure inside the insulation above atmospheric. The leak rates of the IS and top cap were determined to be 3.1 mbar l/s and less than 0.3 mbar l/s respectively, at an overpressure of 6 mbar. Their volumes were measured as well with the IS having a free volume of 4290 l and the top cap of 5750 l, as described in Section 3.1.5. Using the setup given in Section 3.1.4, it was found that the pressure of the insulation could be kept constantly above the atmospheric one with an overpressure of a few millibar, with a flow rate of 50-100 ln/h.

The SGFT chimneys, which constitute a closed volume, were tested for leaks and purged with nitrogen, with a pressure of about 30 mbar above atmospheric. It was found that the pressure inside decreased during the cool down in proportion to the temperature inside, as no pressure regulating mechanism was installed. For future detectors employing this kind of chimney, it is crucial to install an automated pressure regulating system to avoid over- and under-pressures with respect to the atmosphere. The evolution of pressures inside the chimneys can be found in Section 4.2.

6.2 Quality of insulation and temperature evolution during cool down

The insulation of the tank, composed of the IS and the top cap, was found to isolate the tank well from temperature fluctuations in the lab, as shown in Section 3.1. The heat input during operation was calculated to be about 1 kW. However, air gaps in the insulation led to local cold spots on the outer structure and thus the cool down could not be completed. For future detectors employing a similar cryogenic design, it is important to eliminate all such gaps within the insulation and install adequate temperature sensors to detect any arising cold spots.

6.3 Induced signals through capacitive crosstalk

The pulsing measurements on the anode in the detector revealed a level of crosstalk of a few percent on all non-pulsed strips in both views, as described in Section 5.3. This crosstalk is induced through capacitive couplings between the strips. In order to gain a quantitative understanding of these induced signals, capacitance measurements have been performed on one anode module and an equivalent circuit model has been proposed to quantitatively determine the induced currents on non-pulsed strips. We have understood, that the coupling of one strip to ground on one anode module of 50×50 cm^2 really is the sum of its capacitances to all other strips, in both views and thus $C_{det} = 78\,\mathrm{pF} \approx 160 \cdot C_{\perp} + 2 \cdot C_{\parallel} + 2 \cdot C_{\parallel 2} + \cdots$.

The numerically calculated theoretical currents of the equivalent circuit model were compared to the measured currents of a single anode module, with a single strip pulsed. We believe that the equivalent circuit model reproduces well the pulsing and are confident that the capacitive crosstalk is well understood. In addition the measured capacitances between strips, given in Table 5.5, are confirmed by the pulsing measurements. The simulated capacitances given by the COMSOL simulations [27] need to be studied further, as a full simulation of multiple anode strips could provide us with a better understanding of higher order coupling between the strips.

Even though the capacitance between perpendicular strips was found to be only 0.4-0.5 pF, the fact, that each strip couples to 160 perpendicular strips on each anode module, means that this is the main source that provides a constant induced signal on all strips parallel to the pulsed ones, regardless of their respective distance. The crosstalk at the level of the anode is thus conclusively explained by this capacitance to perpendicular strips and hence designs of future anodes could benefit immensely from the reduction of this perpendicular capacitance in terms of minimizing the induced signals. We conclude that the target of future anode designs, with multiple views and equal charge sharing, should be to reduce this capacitance between strips that cross each other. A priori, $C_{\perp}$ is believed to be correlated to the distance between the top layer of the anode and the layer underneath where the individual pixels are connected through wires, as shown in Figure 5.8a. I make the conjecture, that an increase in this distance from the current 1.5 mm would reduce the capacitance between crossing strips and thus minimize the capacitive crosstalk on all strips.

Different induced signals were also observed on the counter connector of the pulsed connector in the readout cards within the SGFT chimneys, as can be seen in Figure 5.9. The exact coupling at this level is not well understood and needs to be studied further.

One of the main drawbacks of the pulsing scheme employed in the $3 \times 1 \times 1$ m^3 detector is that it does not allow to pulse a single strip on the anode. Enabling this option on future detectors would provide a much more accurate way to study the capacitive crosstalk by being able to take full advantage of the readout electronics.

Bibliography

[1] David R. Nygren. Proposal to investigate the feasibility of a novel concept in particle detection. 1974.

[2] C. Rubbia. The Liquid Argon Time Projection Chamber: A New Concept for Neutrino Detectors. 1977.

[3] M. Miyajima, T. Takahashi, S. Konno, T. Hamada, S. Kubota, H. Shibamura, and T. Doke. Average energy expended per ion pair in liquid argon. *Phys. Rev. A*, 9:1438–1443, Mar 1974.

[4] Y.Li et al. Measurement of Longitudinal Electron Diffusion in Liquid Argon. *Nucl. Instrum. Meth.*, A816:160, 2016.

[5] Space charge in ionization detectors. by Sandro Palestini, Kirk T. McDonald, 2007.

[6] A. Rubbia. Future liquid argon detectors. *Nuclear Physics B - Proceedings Supplements*, 235:190 – 197, 2013.

[7] George Bakale, Ulrich Sowada, and Werner F. Schmidt. Effect of an electric field on electron attachment to sulfur hexafluoride, nitrous oxide, and molecular oxygen in liquid argon and xenon. *The Journal of Physical Chemistry*, 80(23):2556–2559, 1976.

[8] C Rubbia et al. Underground operation of the icarus t600 lar-tpc: first results. *Journal of Instrumentation*, 6(07):P07011, 2011.

[9] A. Rubbia. Experiments for CP violation: A Giant liquid argon scintillation, Cerenkov and charge imaging experiment? In *Proceedings of the 2nd NO-VE International Workshop on Neutrino Oscillations: Venice, December 3-5, 2003*, pages 321–350, 2004.

[10] C. Cantini et al. Performance study of the effective gain of the double phase liquid Argon LEM Time Projection Chamber. *JINST*, 10(03):P03017, 2015.

[11] A. Badertscher, A. Curioni, L. Knecht, D. Lussi, A. Marchionni, G. Natterer, F. Resnati, A. Rubbia, and T. Viant. First operation of a double phase LAr Large Electron Multiplier Time Projection Chamber with a two-dimensional projective readout anode. *Nucl. Instrum. Meth.*, A641:48–57, 2011.

[12] C. Cantini et al. Long-term operation of a double phase lar lem time projection chamber with a simplified anode and extraction-grid design. *JINST*, 9:P03017, 2014.

[13] A. Badertscher et al. First operation and performance of a 200 lt double phase LAr LEM-TPC with a 40×76 cm^2 readout. *JINST*, 8:P04012, 2013.

[14] Filippo Resnati. *Modeling, design and first operation of the novel double phase LAr LEM-TPC detector*. PhD thesis, Zürich, 2012.

[15] F. et al. Arneodo. Performance of a liquid argon time projection chamber exposed to the cern west area neutrino facility neutrino beam. *Phys. Rev. D*, 74:112001, Dec 2006.

[16] S. Amerio et al. Design, construction and tests of the {ICARUS} {T600} detector. *Nuclear Instruments and Methods in Physics Research Section A: Accelerators, Spectrometers, Detectors and Associated Equipment*, 527(3):329 – 410, 2004.

[17] André Rubbia. Ardm: a ton-scale liquid argon experiment for direct detection of dark matter in the universe. *Journal of Physics: Conference Series*, 39(1):129, 2006.

[18] H. Chen et al. Proposal for a New Experiment Using the Booster and NuMI Neutrino Beamlines: MicroBooNE. 2007.

[19] André Rubbia. Underground neutrino detectors for particle and astroparticle science: The giant liquid argon charge imaging experiment (glacier). *Journal of Physics: Conference Series*, 171(1):012020, 2009.

[20] Devis Lussi. Study of the response of the novel lar lem-tpc detector exposed to cosmic rays and a charged particle beam. 2013.

[21] R. Acciarri et al. Long-Baseline Neutrino Facility (LBNF) and Deep Underground Neutrino Experiment (DUNE) Conceptual Design Report, Volume 4 The DUNE Detectors at LBNF. 2016.

[22] A Rubbia. Progress report on LBNO-DEMO/WA105 (2015). Technical Report CERN-SPSC-2015-013. SPSC-SR-158, CERN, Geneva, Mar 2015.

[23] B Aimard. Yearly progress report on WA105/ProtoDUNE dual-phase (2017). Technical Report CERN-SPSC-2017-011. SPSC-SR-206, CERN, Geneva, Mar 2017.

[24] S. Amoruso et al. Study of electron recombination in liquid argon with the ICARUS TPC. *Nucl. Instrum. Meth.*, A523:275–286, 2004.

[25] David Montanari, Mark Adamowski, Alan Hahn, Barry Norris, Juergen Reichenbacher, Russell Rucinski, Jim Stewart, and Terry Tope. Performance and results of the lbne 35 ton membrane cryostat prototype. *Physics Procedia*, 67:308 – 313, 2015.

[26] Devis Lussi. Characterization of the novel liquid argon tpc lem-based readout.

[27] Pin-Jung Chiu. Protodune-dp prototype for the deep underground neutrino experiment - dual phase detector.